Manuscript submitted to eLife

Mapping the human subcortical auditory system using histology, post mortem MRI and in vivo MRI at 7T

Kevin Richard Sitek[1,2†]**, Omer Faruk Gulban**[3†]**, Evan Calabrese**[4§]**, G. Allan Johnson**[4]**, Agustin Lage-Castellanos**[3]**, Michelle Moerel**[3,5]**, Satrajit S. Ghosh**[1,2‡]**, Federico De Martino**[3,6‡]

[1]MIT; [2]Harvard University; [3]Department of Cognitive Neuroscience, Faculty of Psychology and Neuroscience, Maastricht University, The Netherlands; [4]Duke University; [5]Maastricht Centre for Systems Biology, Faculty of Science and Engineering, Maastricht University, The Netherlands; [6]Center for Magnetic Resonance Research, University of Minnesota, Minneapolis, USA

*For correspondence:
orcid.org/0000-0001-7761-3727 (OFG);
orcid.org/0000-0002-2172-5786 (KRS)

[†]These authors contributed equally to this work
[‡]These authors also contributed equally to this work

Present address: [§]Department of Radiology, University of California, San Francisco, USA

Abstract   Studying the human subcortical auditory system non-invasively is challenging due to its small, densely packed structures deep within the brain. Additionally, the elaborate three-dimensional (3-D) structure of the system can be difficult to understand based on currently available 2-D schematics and animal models. We addressed these issues using a combination of histological data, post mortem magnetic resonance imaging (MRI), and in vivo MRI at 7 Tesla. We created anatomical atlases based on state-of-the-art human histology (BigBrain) and post mortem MRI (50 μm). We measured functional MRI (fMRI) responses to natural sounds and demonstrate that the functional localization of subcortical structures is reliable within individual participants who were scanned in two different experiments. Further, a group functional atlas derived from the functional data locates these structures with a median distance below 2mm. Using diffusion MRI tractography, we revealed structural connectivity maps of the human subcortical auditory pathway both in vivo (1050 μm isotropic resolution) and post mortem (200 μm isotropic resolution). This work captures current MRI capabilities for investigating the human subcortical auditory system, describes challenges that remain, and contributes novel, openly available data, atlases, and tools for researching the human auditory system.

Introduction

Understanding the structure of the human subcortical auditory pathway is a necessary step to research its role in hearing, speech communication, and music. However, due to methodological issues in human research, most of our understanding of the subcortical (thalamic, midbrain, and brainstem) auditory pathway arises from research conducted in animal models. This might be problematic because, while the organization of the auditory pathway is largely conserved across mammalian species (*Malmierca and Hackett, 2010*; *Schofield, 2010*), the form and function of each structure may not be analogous (*Moore, 1987*). In this paper we show that three human imaging modalities -histology, post mortem magnetic resonance imaging (MRI), and in vivo MRI at ultra high-field (7 Tesla)- can identify the structures of the subcortical auditory pathway at high spatial resolution (between 50 and 1100 μm).

    Although MRI has become increasingly powerful at imaging deep brain structures, anatomical

Manuscript submitted to eLife

investigation of the human subcortical auditory pathway has been primarily conducted in post mortem tissue dissection and staining. *Moore* (*1987*) stained both myelin and the cell bodies of subcortical auditory structures in four post mortem human brainstem samples and compared them to the analogous structures in cats (a common model for auditory investigations at the time). Later investigations from the same group (*Moore et al., 1995*) used myelin and Nissl cell body staining to investigate the timeline of myelination in human auditory brainstem development. More recently, *Kulesza* (*2007*) stained six human brainstems for Nissl substance, focusing on the superior olivary complex, finding evidence of a substructure (the medial nucleus of the trapezoid body) whose existence in the human auditory system has been debated for decades.

Advances in post mortem human MRI allow for investigating three-dimensional (3-D) brain anatomy with increasingly high resolution (100 μm and below). This points to "magnetic resonance histology" (*Johnson et al., 1993*) as a promising avenue for identifying the small, deep subcortical auditory structures. However, to the best of our knowledge, post mortem MRI has not been utilized within the subcortical auditory system, although it has provided useful information about laminar structure in the auditory cortex (*Wallace et al., 2016*).

To study the subcortical auditory system in living humans, MRI is the best available tool due to its high spatial resolution. Anatomical in vivo MRI investigations of the human subcortical auditory pathway so far have focused on thalamic nuclei (*Devlin et al., 2006*; *Moerel et al., 2015*), and the identification of the acoustic radiations between the auditory cortex and medial geniculate nucleus of the thalamus with diffusion-weighted MRI tractography (*Devlin et al., 2006*; *Behrens et al., 2007*; *Javad et al., 2014*; *Maffei et al., 2018*). Due to their small size and deep locations, identification of more caudal subcortical structures-the superior olivary complex and cochlear nucleus-remain challenging with in vivo anatomical MRI.

Although lower spatial resolution than anatomical MRI, functional MRI (fMRI) has been used to investigate the relevance of subcortical processing of auditory information in humans, but it has been limited by the small size of the structures involved and the relatively low resolution attainable at conventional field strengths (3 Tesla and below) (*Guimaraes et al., 1998*; *Harms and Melcher, 2002*; *Griffiths et al., 2001*; *Hawley et al., 2005*). These acquisitions required trade-offs, such as low through-plane resolution (7 mm) in exchange for moderate in-plane resolution (1.6 mm), and in some cases researchers synchronized image collection to the cardiac cycle in order to overcame the physiological noise associated with blood pulsation in the brainstem (*Guimaraes et al., 1998*; *Sigalovsky and Melcher, 2006*).

More recent advances in MRI, especially the increased signal-to-noise ratio (SNR) available at ultra-high magnetic fields (7 Tesla and above), have enabled higher resolution functional imaging of subcortical structures and more advanced localization of human auditory subcortical structures as well as their functional characterization. Using MRI at 7 Tesla (7T), *De Martino et al.* (*2013*) and *Moerel et al.* (*2015*) collected relatively high resolution (1.1-1.5 mm isotropic) fMRI with an auditory paradigm to identify tonotopic gradients in the inferior colliculus and medial geniculate nucleus. In these studies, high isotropic resolution and SNR provided an opportunity to investigate auditory responses throughout the subcortical auditory system.

Despite the methodological advances in investigating the human brain, a systematic comparison of their capabilities for imaging the subcortical auditory system has not yet been undertaken. Here we use publicly available histological data (*Amunts et al., 2013*) to segment the main nuclei along the subcortical auditory pathway. Using state-of-the-art acquisition and analysis techniques, we evaluate the ability of identifying the same structures through post mortem anatomical MRI, through functional MRI using natural sounds, and through estimating the connectivity between subcortical auditory structures with post mortem and in vivo diffusion MRI tractography. To compare the histological, post mortem, and in vivo data, we project all images to MNI common reference space (*Fonov et al., 2009*, *2011*). Finally, to facilitate dissemination of our results, we have made the post mortem anatomical data, in vivo functional and diffusion data, and the resulting atlases publicly available.

Manuscript submitted to eLife

92   Where histology provides ground truth information about neural anatomy, we show that post
93   mortem MRI can provide similarly useful 3-D anatomical information with less risk of tissue damage
94   and warping. We also show that in vivo functional MRI can reliably identify the subcortical auditory
95   structures within individuals, even across experiments. Overall, we found that each methodology
96   successfully localized each of the small structures of the subcortical auditory system, and while
97   known issues in image registration hindered direct comparisons between methodologies, each
98   method provides complementary information about the human auditory pathway.

99   **Results**

100   **Definition of a subcortical auditory atlas from histology**
101   To obtain a spatially accurate reference for all the subcortical auditory structures, we manually
102   segmented publicly available histological data (100 μm version of the BigBrain 3-D Volume Data
103   Release 2015 in MNI space from https://bigbrain.loris.ca (*Amunts et al., 2013*)).
104   Upon inspecting this dataset, we noticed that the area around the inferior colliculus was incor-
105   rectly transformed into MNI space. This was causing the colliculi to be larger and more caudal than
106   in the MNI reference brain (Fig 8, second and third panels). Thus, our first step was to correctly
107   register the area around the colliculi (Fig 8, fourth panel; see Methods for details on the correction
108   procedure).
109   The results of our BigBrain subcortical auditory segmentation in corrected MNI space are
110   reported in Fig 1 together with schematics redrawn from *Moore* (*1987*) (for the cochlear nucleus,
111   superior olivary complex, and inferior colliculus) and the Allen Human Brain Atlas (*Hawrylycz et al.,*
112   *2012*; *Ding et al., 2016*) (for the medial geniculate body). These schematics were used as reference
113   during the segmentation. The 3-D rendering of the segmented structures highlighting the complex
114   shape of the cochlear nucleus and superior olivary complex is also presented in Fig 1. The rendering
115   is presented from a posterior lateral view in order to compare it with the Gray's Anatomy, Plate 719
116   (*Gray and Lewis, 1918*).

117   **Post mortem MRI**
118   Post mortem MRI atlas of the human subcortical auditory system
119   Magnetic resonance histology—i.e., the study of tissue at microscopic resolution using MRI—provides
120   several unique advantages over conventional histology: 1) it is non-destructive; 2) it suffers minimal
121   distortion from physical sectioning and dehydration; 3) it yields unique contrast based on water
122   in the tissue and how it is bound (e.g., diffusion); and 4) it produces 3-D data. These advantages
123   make it an ideal medium for visualizing the 3-D organization of the deep brain structures (*Johnson*
124   *et al., 1993*). To delineate the subcortical auditory structures with MR histology, we acquired 50 μm
125   isotropic voxel size 3-D gradient echo (GRE) MRI on a human post mortem brainstem and thalamus
126   (described previously in (*Calabrese et al., 2015*); see Methods for additional details). These data are
127   presented in Figure 2 (second column) after transformation to MNI space and resampling to 100
128   μm isotropic resolution (see Methods section for details). The post mortem MRI data are presented
129   together with the histological data for comparison (first column).
130   Based on our segmentations of the subcortical auditory structures in the post mortem MRI
131   data, the resulting 3-D model is presented in Fig 2. A volumetric quantification of the identified
132   structures (in the BigBrain and post mortem MRI) is reported in Table 3 and the overlap between
133   the segmentations computed after projection in MNI space are reported in Table 2 (as inset in Fig 2).

134   3-D connectivity map of the human subcortical auditory system from post mortem
135   diffusion MRI
136   Identifying the connectivity between subcortical auditory nuclei is crucial for understanding the
137   structure of the pathway. However, methods for tracing neuronal pathways that are available in
138   other animal models are generally not available in human studies, even post mortem. Diffusion-
139   weighted MRI (dMRI) can be used to measure the orientation and magnitude of molecular motion
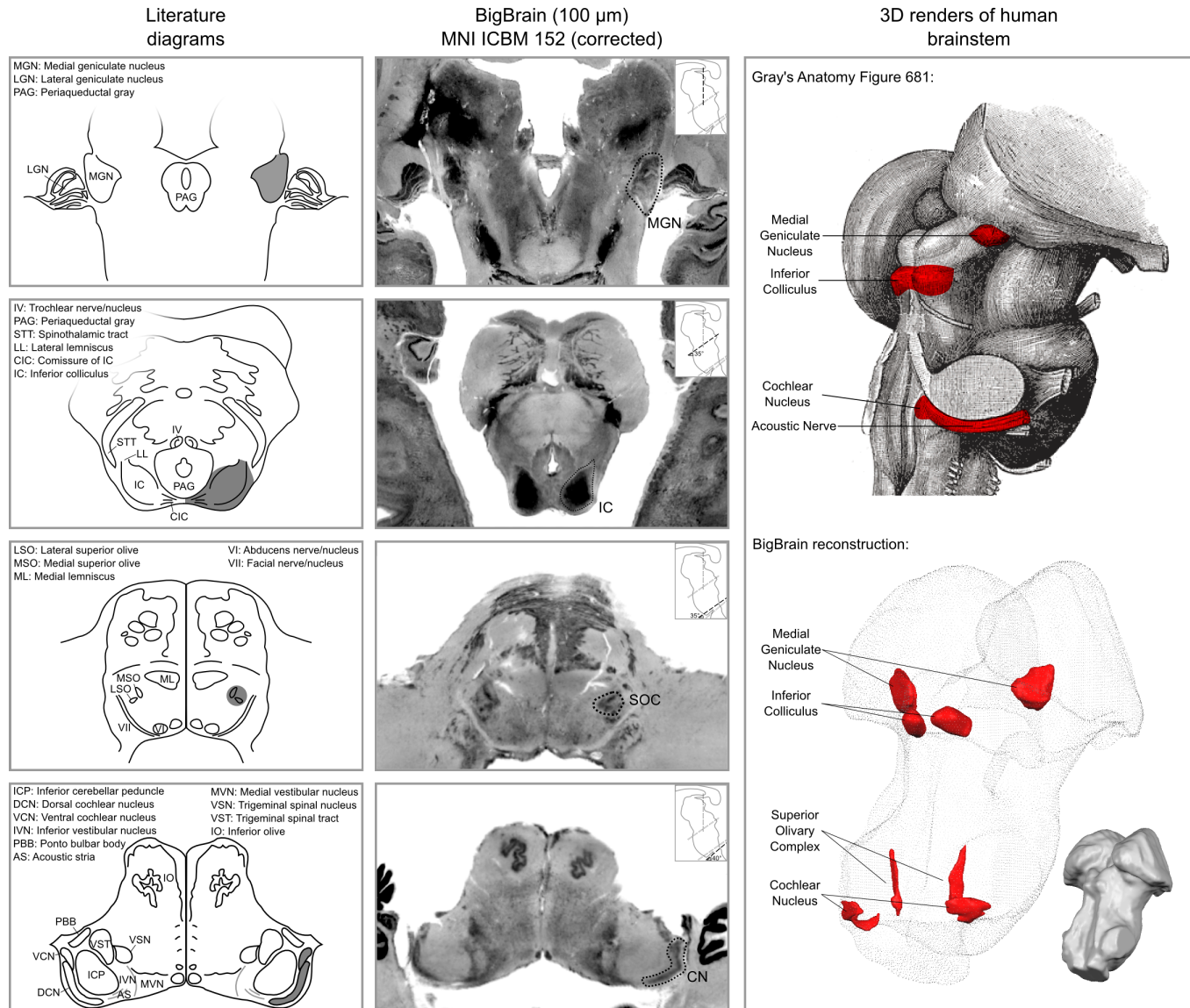
Manuscript submitted to eLife

Figure 1. Literature diagrams (left columns) redrawn from *Moore* (*1987*) for the cochlear nucleus (CN), superior olivary complex (SOC), inferior colliculus (IC) and from the Allen Human Brain Atlas (*Hawrylycz et al., 2012*) for the medial geniculate body (MGB) compared to similar cuts from histology (BigBrain) in MNI (central column) and 3-D reconstructions of the segmented structures from the histology (bottom right column). The auditory structures are highlighted in gray in the left column, by a dotted line in the central column and in red on the modified Gray's anatomy Plate 719 (*Gray and Lewis, 1918*) and rendered as solid red surface meshes within the surface point cloud render of BigBrain MNI brainstem (right column). See Figure 9 for 3-D animated videos of these auditory structures.
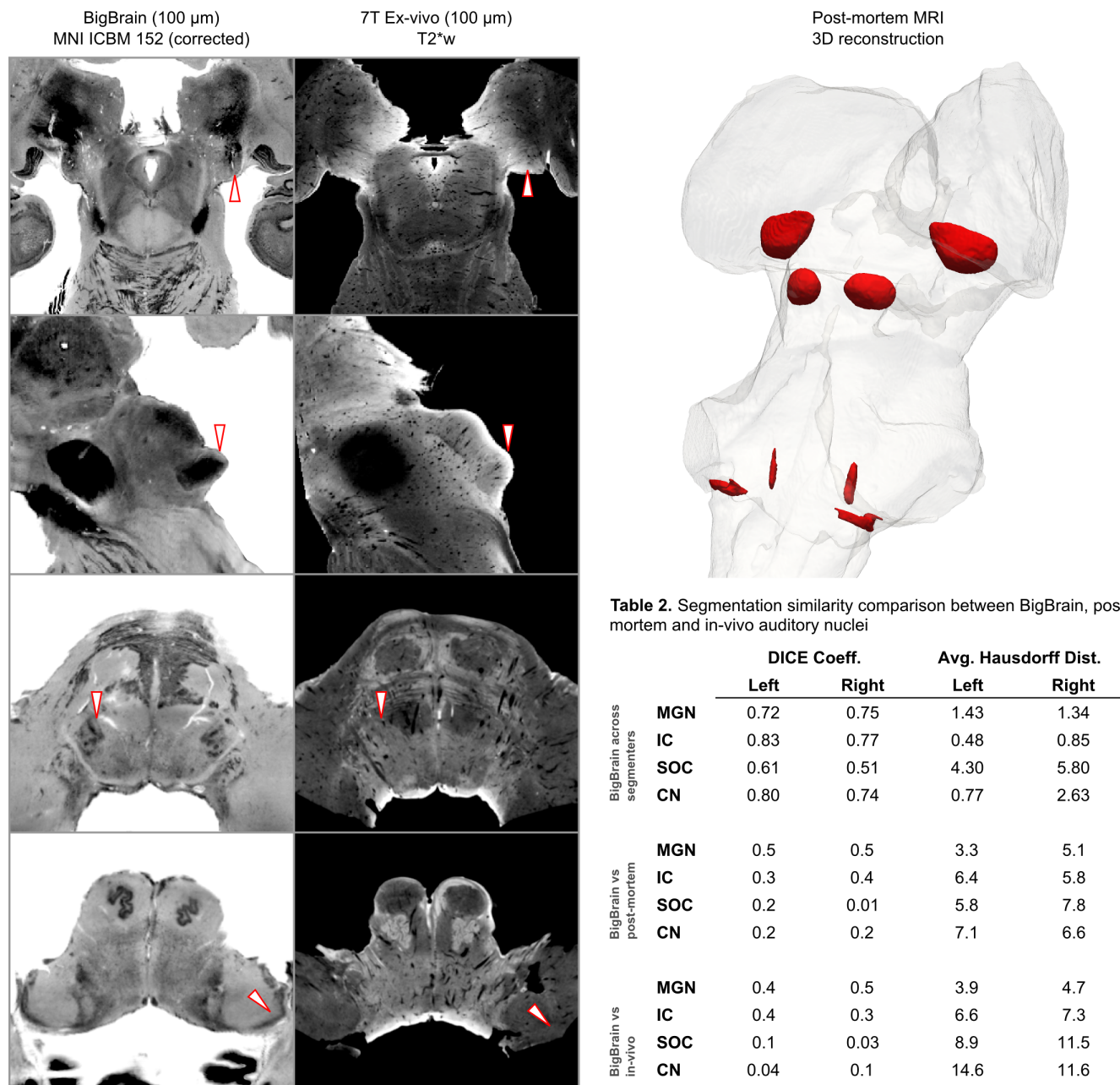
Manuscript submitted to eLife

BigBrain (100 μm)
MNI ICBM 152 (corrected)

7T Ex-vivo (100 μm)
T2*w

Post-mortem MRI
3D reconstruction

Table 2. Segmentation similarity comparison between BigBrain, post-mortem and in-vivo auditory nuclei

		DICE Coeff.		Avg. Hausdorff Dist.	
		Left	Right	Left	Right
BigBrain across segmenters	MGN	0.72	0.75	1.43	1.34
	IC	0.83	0.77	0.48	0.85
	SOC	0.61	0.51	4.30	5.80
	CN	0.80	0.74	0.77	2.63
BigBrain vs post-mortem	MGN	0.5	0.5	3.3	5.1
	IC	0.3	0.4	6.4	5.8
	SOC	0.2	0.01	5.8	7.8
	CN	0.2	0.2	7.1	6.6
BigBrain vs in-vivo	MGN	0.4	0.5	3.9	4.7
	IC	0.4	0.3	6.6	7.3
	SOC	0.1	0.03	8.9	11.5
	CN	0.04	0.1	14.6	11.6

Figure 2. BigBrain–7T post mortem MRI image comparisons. Histological data (BigBrain) (left column) and T2*-weighted post mortem MRI data (100 μm - central column) in MNI space. Panels from bottom to top are chosen to highlight subcortical auditory structures (CN [bottom] to MGB [top]). Arrows (white with red outline) indicate the location of the subcortical auditory nuclei. The 3-D structures resulting from the segmentation of the post mortem data is presented on the top right panel. Table 2 quantifies (using DICE coefficient and average Hausdorff distance) the agreement (in MNI space) for all subcortical structures between: 1) segmentations performed on the BigBrain dataset by the two raters (KS and OFG) [top]; 2) segmentations obtained from the BigBrain dataset and from the post mortem MRI data [middle]; 3) segmentations obtained from the BigBrain dataset and from in vivo functional MRI data [bottom]). See Figure 9 for 3-D animated videos of these auditory structures.

Table 1. Volume comparisons (mm3) across different segmentations of the auditory brainstem regions of interest.

	Literature	BigBrain MNI	Post-mortem	In-vivo (thr=3)	In-vivo (thr=4)	In-vivo (thr=5)
CN	46	32	11	54	24	11
SOC	7	6	4	124	63	29
IC	65	63	73	263	189	146
MGN	58	75	134	304	207	152

Figure 3. Comparisons between the volume of auditory subcortical structures reported in the literature (*Glendenning and Masterton, 1998*) and the volume obtained in our BigBrain segmentation (in MNI space), post mortem MRI data segmentation and in vivo functional clusters (defined based on voxels that are significant in at least three, four, or five participants out of the ten included in Experiment 1).

140   and infer patterns of white matter in brain tissue (both post mortem and in vivo). Using 200 μm
141   diffusion-weighted MRI data acquired on the same post mortem sample (see Methods for details),
142   we modeled diffusion orientations and estimated likely connectivity pathways (or streamlines) using
143   tractography. Constraining the streamlines to only those that pass through auditory structures (as
144   identified from the anatomical MRI data and dilated 500 μm to include adjacent white matter), we
145   visualized the connectivity map of the subcortical auditory pathway in Fig 4, left panel.

146   Connectivity closely resembles the expected pattern of the human subcortical auditory wiring.
147   In particular, streamlines predominantly pass through the lateral lemniscus, the primary subcortical
148   auditory tract. Additional streamlines run through the brachium of the inferior colliculus, connecting
149   the inferior colliculus with the medial geniculate of the thalamus. Many streamlines then course
150   rostrally toward the auditory cortex (not present in this specimen).

151   At the caudal extent of the lateral lemniscus, streamlines pass through the superior olivary
152   complex. Streamlines also run through the root of CNVIII. In total, each expected step along the
153   subcortical auditory pathway is represented in this connectivity map.

154   Fig 4 (top right panel) shows the percentage of total streamlines connecting each of the sub-
155   cortical auditory structures as estimated from this post mortem diffusion MRI sample. Overall,
156   connections tend to be between ipsilateral structures, with weak connectivity to contralateral
157   structures other than commissural connections to the contralateral homolog (except for between
158   the cochlear nuclei). Still, the majority of streamlines pass through just one region (shown along the
159   diagonal).

160   To investigate the relationship between streamline connectivity and ROI definition strictness,
161   we conducted two additional analyses. In Fig 4, we dilated the anatomical ROIs by 500 μm (2.5
162   voxels at 200 μm resolution), thereby including nearby white matter tracts (as well as adjacent
163   subcortical structures). In contrast, Fig 4 Supplement 1 shows streamlines based on the anatomical
164   ROIs without dilation to account for white matter. As regions were defined as the core nuclei in the
165   anatomical MRI, they largely exclude white matter tracts (such as the lateral lemniscus and brachium
166   of the inferior colliculus), leading to much sparser connectivity between subcortical auditory nuclei.

167   Next, we resampled the diffusion MRI images to an in vivo-like resolution (1.05 mm isotropic). We
168   again estimated fiber ODFs using CSD and estimated white matter connections with deterministic
169   tractography. Using the (undilated but downsampled) anatomically defined ROIs as tractogra-
170   phy waypoints, we can visualize streamline estimates connecting subcortical auditory structures
171   (Fig 4 Supplement 2). Similar to the dilated ROI connectivity estimates, we see greater ipsilateral
172   connectivity estimates between structures, particularly between left structures.

Vasculature representations from post mortem MRI

174   Because T2*-weighted GRE imaging is sensitive to blood vessels, we processed our anatomical MR
175   image to highlight brainstem vasculature (Fig 6, right column, base image). These 3-D vasculature
176   images bear striking resemblance to post mortem data acquired with a stereoscopic microscope
177   after full clearing method (see *Duvernoy* (*2013*) for detailed diagrams of human brainstem vascula-
178   ture). These vasculature images in the MNI space can be helpful to understand the nature of the in
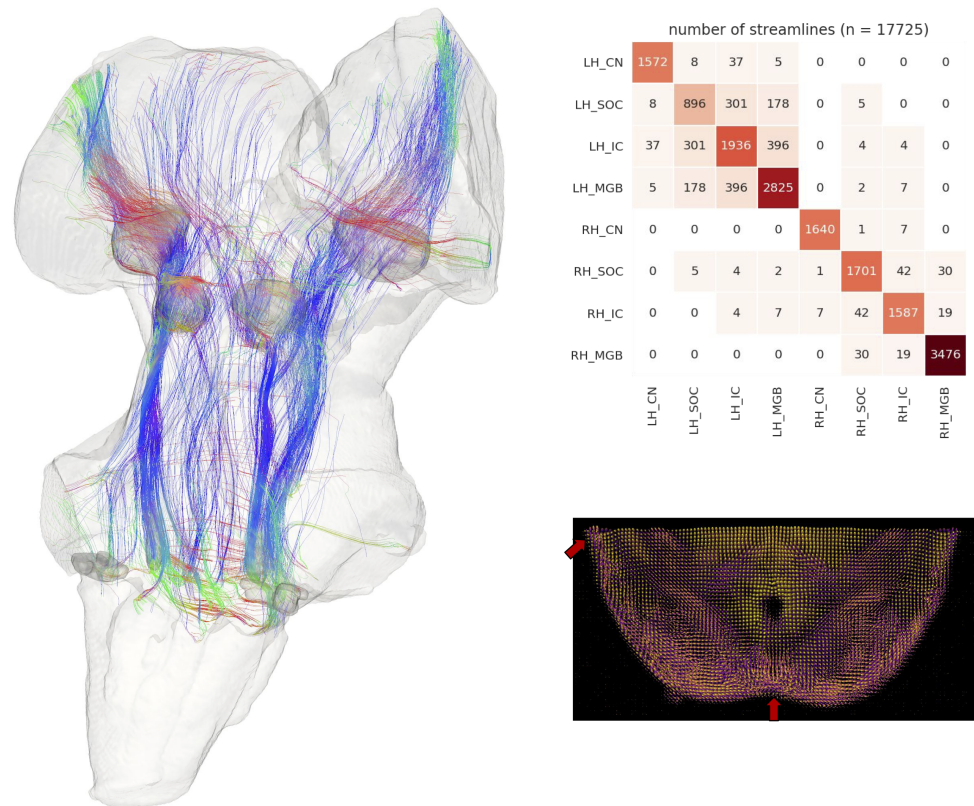
Manuscript submitted to eLife

Figure 4. Post mortem diffusion MRI tractography. Left: streamlines passing through subcortical auditory structures, defined from 50 μm post mortem MRI in the same specimen, warped to 200μm isotropic diffusion image space and dilated 2.5 voxels (500 μm) to include neighboring white matter. Colors represent the local orientation at each specific point along the streamline: blue is inferior-superior, red green is anterior-posterior, and red is left-right. Ten percent of streamlines are represented in this image. A rotating animation is available in the online resources. Top right: Connectivity heatmap of subcortical auditory structures. Bottom right: Diffusion orientation distribution functions (ODFs) for each voxel; axial slice at the level of the rostral inferior colliculus (IC), including the commisure of the IC (bottom center arrow) and brachium of the IC (top left arrow). A video of the streamlines is available online: https://osf.io/kmbp8/

Figure 4–Figure supplement 1. Post mortem tractography with undilated ROIs.

Figure 4–Figure supplement 2. Post mortem tractography using data downsampled to in vivo resolution (1.05 mm).

Figure 4–video 1. 360° rotation video of post mortem streamlines.

179   vivo functional signals (see next section).

In vivo MRI

181 We next sought to identify the structures and connections of the human subcortical auditory
182 system in living participants. By leveraging the increase signal and contrast to noise available at
183 ultra-high magnetic fields (7 Tesla) (*Vaughan et al., 2001*; *Ugurbil et al., 2003*; *Ugurbil, 2016*), we
184 collected high resolution anatomical (0.7 mm isotropic), diffusion-weighted (1.05 mm isotropic;
185 198 diffusion gradient directions across 3 gradient strengths) and functional (1.1 mm isotropic)
186 MRI in ten participants (see Methods for details). Leveraging the increased SNR available at high
187 fields, we aimed to collect data that would allow a functional definition of the auditory pathway
188 in individual participants. For this reason, we collected a large quantity of functional data in all
189 individuals: two sessions with 12 runs each in Experiment 1 and two sessions with eight runs each
190 in Experiment 2 (totalling 8 hours of functional data for each participant who completed both
191 experiments). All statistical analyses were performed at the single subject level. Group analyses
192 were used to evaluate the correspondence across subjects of individually defined regions (i.e., the
193 definition of a probabilistic atlas across participants) as well as the ability to generalize to new
194 participants by means of a leave-one-out analysis.

Anatomical MRI

196 Visual inspection and comparison to the MNI dataset (Supp. Fig 2) showed that the MGB and IC
197 could be identified on the basis of the anatomical contrast, especially in the short inversion time
198 T1-weighted data (*Tourdias et al., 2014*; *Moerel et al., 2015*). However, while the superior olivary
199 complex (SOC) could be identified in the MNI dataset (Supp. Fig 2), it could not be identified in
200 average anatomical image from our 7T data. This is possibly due to the limited number of subjects
201 leading to the lower signal to noise in the average image. We have also explored the combination
202 of image contrasts within each individual using a compositional method proposed in (*Gulban et al.,*
203 *2018b*), but the results were inconclusive.

Functional MRI

205 The difficulty in delineating the CN and SOC from anatomical in vivo MRI data (see Fig 1 for the
206 average anatomical images obtained from our in vivo data) oriented our investigation towards the
207 possibility of identifying the subcortical auditory pathway—in vivo and in single individuals—on
208 the basis of the functional responses to sounds. Functional responses to 168 natural sounds
209 (Experiment 1) were collected at 7T using a sparse acquisition scheme and a fast even related
210 design. We additionally report the reproducibility of the individual functional delineations in six
211 out of the ten participants who participated in a follow up experiment in which responses to 96
212 natural sounds (Experiment 2) were collected at 7T using a sparse acquisition scheme and a fast
213 even related design.

214   Statistical analysis of the functional responses allowed us to define voxels with significant
215 activation in response to sounds in each individual. Additionally, we created a probabilistic functional
216 atlas based on the overlap of statistically significant maps across individuals (after anatomical
217 registration to a reference subject). To evaluate the generalization to new data we also computed
218 leave-one-out probabilistic functional atlases each time leaving one one of our participants (see
219 Methods for details).

220   Figure 5 shows, for each individual participant, the statistically thresholded (see Methods)
221 activation maps together with leave-one-out probabilistic functional maps obtained considering
222 all other individuals. The unthresholded maps are reported in supplement videos to Figure 5
223 and available for inspection in the online repository of the data. In all our participants, we could
224 identify clusters of significant activation in response to sounds in the MGB, IC, SOC, and CN. In each
225 individual and for each auditory nucleus, these activation clusters correspond to locations that are
226 significantly active in at least three out of the other nine participants to the experiment. Figure
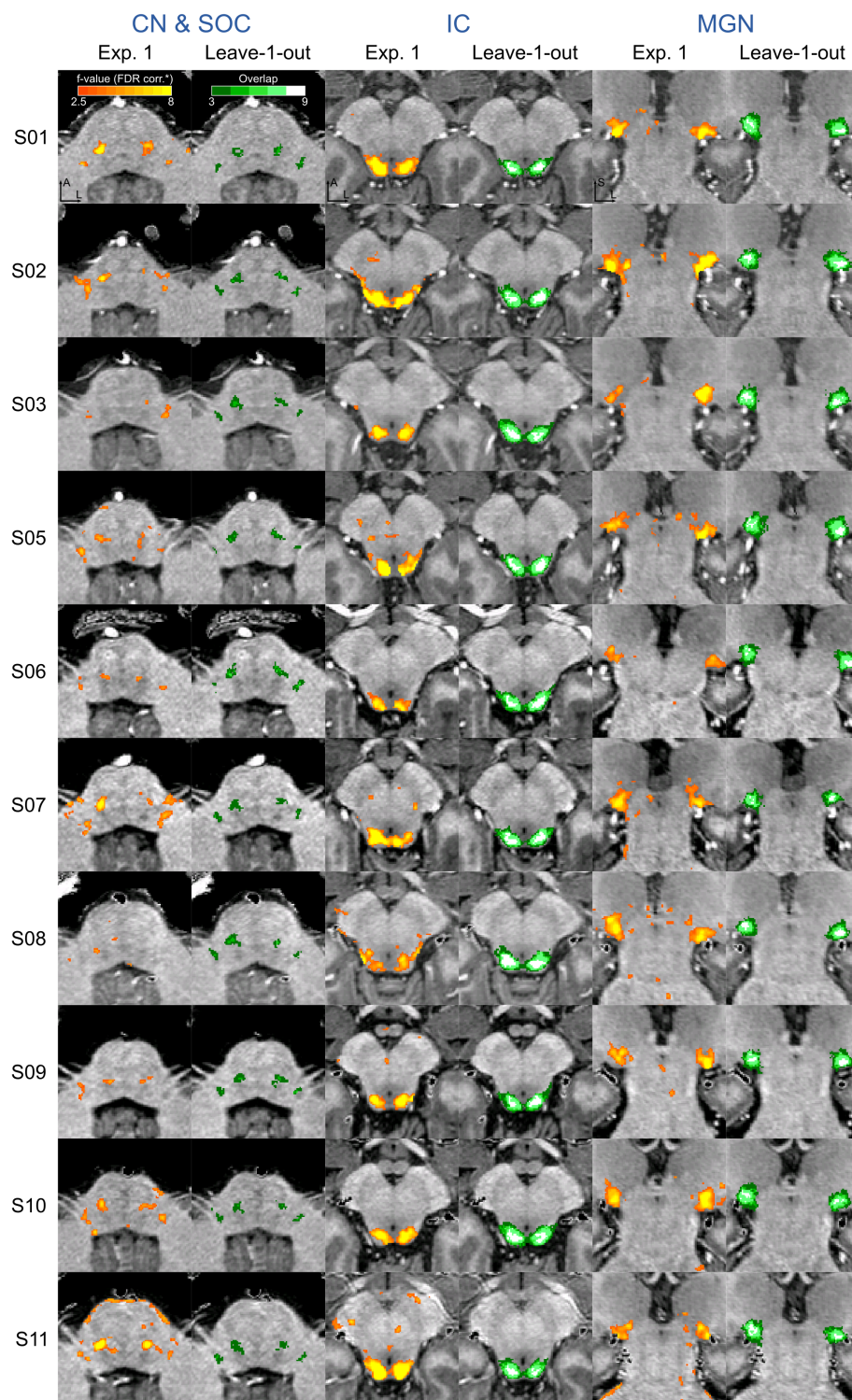
Manuscript submitted to eLife

Figure 5. Single subject functional activation maps obtained from Experiment 1 thresholded for significance (FDR-q = 0.05 and p<0.001; see Methods for details) and leave-one-out probabilistic functional maps highlighting voxels that are significant in at least three of the other nine subjects. For each participant, CN/SOC and IC are shown in transversal cuts, MGB is shown in a coronal cut. See single subject videos for 3-D view of these maps in Figure 10 supplements. Unthresholded maps can be found in our online resources (see Data Availability section).

Figure 5–Figure supplement 1. Correspondence between single subject activation maps and leave-one-out probabilistic maps.

Figure 5–Figure supplement 2. Effect of threshold on leave-one-out probabilistic maps on correspondence with single subject activations

Figure 5–Figure supplement 3. Reproducibility across experiments of the functional activation maps in six participants (also see Figure 11).

Figure 5–Figure supplement 4. Correspondence between single subject activation maps across experiments.

Figure 5–Figure supplement 5. Effect of spatial smoothing in the analysis of the data collected from two of the participants.

227 Supplement 1 to Figure 5 reports the overlap and distance between functional centroids of the single
228 subject activation maps and the leave-one-out probabilistic maps. In addition, Figure Supplement 3
229 to Figure 5 shows the reproducibility of the functional responses across experiments in six of the
230 participants. The analysis of the overlap and distance between the centroids of activation across
231 experiments within each of these six participants is reported in Figure supplement 4 to Figure
232 5. The higher signal-to-noise ratio attainable in regions corresponding to the IC and MGB results
233 in highly reproducible functional responses both within and across participants in these regions.
234 Activation clusters identified at the level of CN and SOC in single individuals also reproduce (albeit
235 to a smaller degree with respect to IC and MGB), both within subjects (i.e. across experiments) and
236 across subjects.

237 The left column of Figure 6 shows the probabilistic functional map obtained from all participants
238 in Experiment 1 (i.e., representing the number of subjects in which each voxel was identified as
239 significantly responding to sounds-the map is thresholded to display voxels that are significantly
240 activated in at least three out of the ten participants) overlaid on the in vivo average anatomical MRI
241 image (short inversion time T1-weighted image (*Tourdias et al., 2014*); see Methods for details).

242 Projecting these data to the reference MNI space allowed evaluating the correspondence
243 between in vivo functionally defined regions and histological data (Big Brain - Figure 6, center
244 column).

245 At the level of the CN, the clusters of voxels active in at least three out of the ten participants
246 correspond mostly to the ventral part of CN. The dorsal subdivision of the CN is not recovered
247 in these probabilistic maps (at least not in at least three volunteers consistently) possibly due to
248 partial voluming with the nearby cerebrospinal fluid in combination with thinness (thickness around
249 0.5 mm) of the dorsal CN as it wraps around inferior cerebellar peduncle (see Fig 1). Nearby, the
250 location of the activation clusters identifying the SOC overlaps with the SOC as identified in the
251 BigBrain data.

252 As the next step, we qualitatively investigated if the orientation of the vasculature at the level of
253 the SOC may have an effect on size (and location) of the functionally defined regions. As a visual aid
254 in this evaluation, we overlaid the functionally defined regions with the vasculature image obtained
255 from the post mortem data (Fig 6, right column). In all subcortical regions the vasculature appears
256 to have a specific orientation, and, at the level of the SOC, vessels drain blood from the center in a
257 ventral direction (i.e., the direction of draining is towards the surface of the brainstem in the top of
258 the image reported in the transverse view, bottom in Fig 6). This specific vasculature architecture
259 may result in the displacement or enlargement of the functionally defined clusters towards the
260 ventral surface of the brainstem (as highlighted in the correspondence with histological data in
261 Fig 6).

262 The probability of the same voxel to be significantly modulated by sound presentation across
263 subjects increased at the level of the IC and MGB, where the histologically defined regions cor-
264 responded (for the large part) to all subjects exhibiting significant responses to sounds. At the
265 threshold of three subjects in the probabilistic maps, the IC seems to extend towards the superior
266 direction, bordering and sometimes including parts of superior colliculus. On the other hand,
267 similarly to what may happen in the SOC, the general directions of the vasculature penetrating the
268 IC and draining blood towards the dorsal surface of brainstem angled in a superior direction (Fig 6
269 right panel) may also impact the functional definition of the IC.

270 The functional responses in the MGB cover an area that is in agreement with histological data.
271 Interestingly, compared to the IC or SOC, there is no major direction of extension of functional
272 responses as well as no clear direction (in comparison to SOC and IC) of vascular draining.

273 A quantification of the volume of functionally defined structures is reported in Table 3 for
274 different thresholds of the probabilistic group map (from a threshold that defines the regions
275 based on voxels that are significant in at least three out of the ten participants to a threshold that
276 define the regions based on voxels that are significant in at least five out of the ten participants).
277 The overlap between functional regions and the BigBrain segmentations after projection in MNI

278 space is reported in Table 2 (as bottom right inset in Fig 2 - computed using a threshold for the
279 probabilistic maps that defines the regions based on voxels that are significant in at least three of
280 the ten participants).

Diffusion MRI

282 With the successful identification of the subcortical auditory structures with functional MRI, we next
283 sought to estimate the likely connections between these structures in vivo. We analyzed the high
284 spatial and angular resolution diffusion data to estimate streamlines of white matter connectivity
285 following a similar process as the post mortem MRI (see Methods for further details).

286 Fig 7 shows diffusion tractography streamlines that pass through at least one subcortical auditory
287 structure (as defined by group-level probabilistic functional activation [significant response in at
288 least three out of ten subjects]; see section above). The high spatial and angular resolution of these
289 data allow for vastly improved estimation of white matter connections between these deep, small
290 structures.

291 While not a measure of actual physical brain connections—and therefore requiring caution in
292 interpretation—connectivity patterns resemble what we would expect to see based on animal model
293 tracer investigations. Overall, the connectivity network appears to be dominated by laterality, in that
294 left hemisphere structures are generally more connected with other left hemisphere structures.

295 However, there are a few notable exceptions to this pattern: the cochlear nuclei and superior
296 olivary complexes are strongly connected bilaterally, which fits with animal research suggesting
297 one-half to two-thirds of ascending auditory connections cross the midline at these early stages.
298 Additionally, there are a small number of connections between left and right inferior colliculi, likely
299 along the anatomical commissure of the inferior colliculus.

Discussion

301 The auditory pathway includes a number of subcortical structures and connections, but identifying
302 these components in humans has been challenging with existing in vivo imaging methods. We
303 showed that functional localization of the subcortical auditory system is achievable within each
304 participant, and that localization is consistent across experimental sessions. To further facilitate
305 research on the anatomy and function of the human subcortical auditory system, we created
306 3-D atlases of the human auditory pathway based on gold standard histology, 50 μm isotropic
307 resolution post mortem anatomical MRI, and in vivo functional MRI at 7T. In addition, we created
308 3-D connectivity maps of the human subcortical auditory pathway using diffusion MRI tractography
309 in a post mortem MRI sample and in living participants.

310 These atlases and connectivity maps are the first fully 3-D representations of the human
311 subcortical auditory pathway and are publicly available to make the localization of subcortical
312 auditory nuclei easier. In particular, the atlases are available in a common reference space (MNI152)
313 to make registration to other MRI data as straightforward as possible. As part of this registration
314 process, we have improved the registration of the brainstem of BigBrain histological data to the
315 MNI space, where the original MNI version presented a significant misregistration of the colliculi (as
316 noticeable in Fig 8). The result of our new registration allows to more correctly localize the colliculi
317 of BigBrain data in MNI without compromising the registration of other brainstem and thalamic
318 nuclei.

319 In creating the atlas with three distinct modalities, we were able to assess the reliability of each
320 of the methods in identifying the human subcortical auditory pathway. Each modality provided
321 useful information to the segmentation of the auditory nuclei. All regions could be identified in
322 the BigBrain histological data, that also allowed us to identify small auditory sub-nuclei such as
323 the medial superior olive and lateral superior olive. High-resolution post mortem MRI also clearly
324 delineated the medial geniculate and inferior colliculus (with less contrast for the superior olive
325 and cochlear nucleus), while the overall image contrast facilitated registration with in vivo MRI.
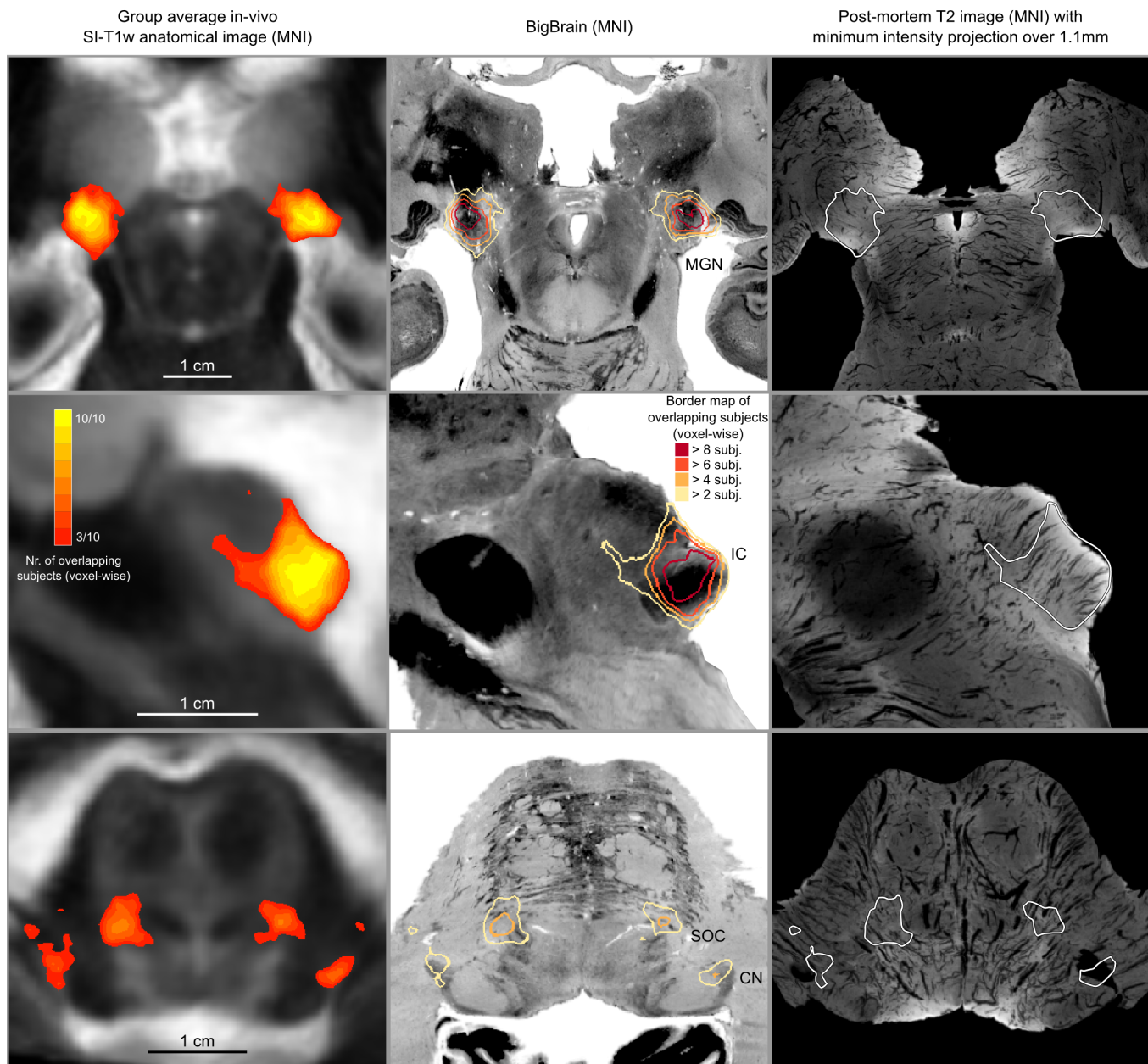326 High-resolution in vivo functional MRI exhibited greater sensitivity to auditory structures than in

Figure 6. In vivo functional MRI responses to auditory stimuli, combined across ten participants. Left column: Conjunction of participants plotted on top of one participant's short inversion T1-weighted anatomical MRI. Center column: Conjunction of participants' fMRI responses warped to MNI space and plotted on top of BigBrain MNI (corrected) image. Right column: Conjunction of fMRI responses plotted on top of post mortem MRI vasculature images (1.1 mm minimum intensity projection).
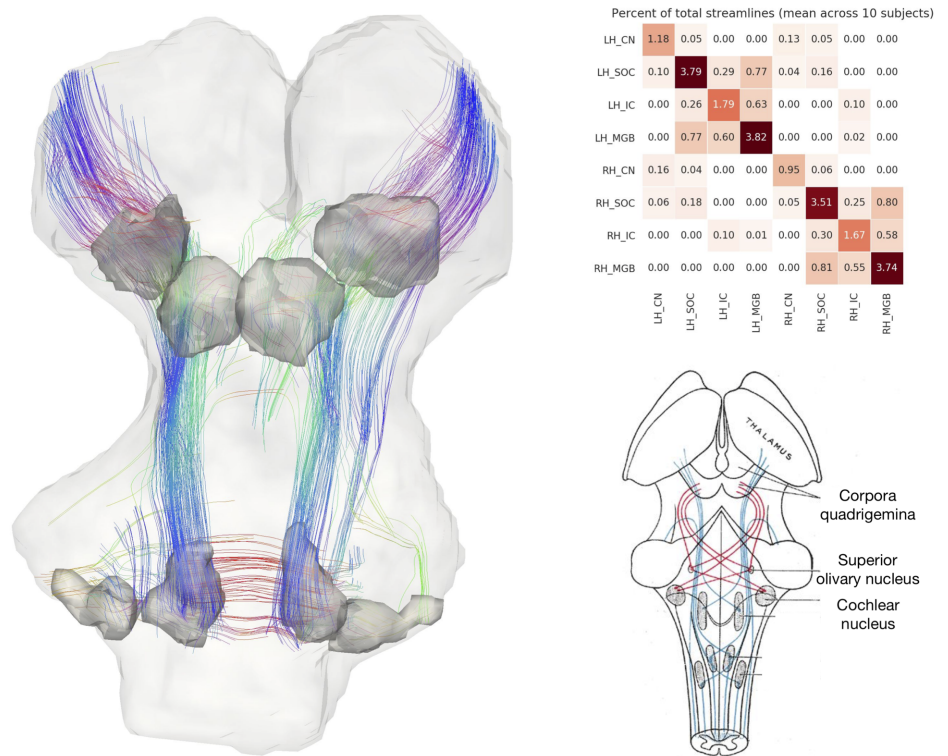
Manuscript submitted to eLife

Figure 7. In vivo tractography of the subcortical auditory system from 7T diffusion-weighted MRI. Left: 3-D images from one participant. Fiber orientation distribution functions were estimated from diffusion-weighted MRI images of the brainstem and were used for deterministic tractography. Streamlines that passed through functionally defined auditory ROIs (dark grey) are shown here (excluding streamlines through the medulla). Colors represent the local orientation at each specific point along the streamline: blue is inferior-superior, red green is anterior-posterior, and red is left-right. A rotating animation is available in the online resources. Top right: connectivity between subcortical auditory ROIs as a percentage of total brainstem streamlines, averaged over 10 participants. Bottom right: schematic of auditory brainstem connectivity from Gray's Anatomy of the Human Body. A video of the streamlines is available online: https://osf.io/ykd24/

Figure 7–Figure supplement 1. Bar plot of streamline counts through each ROI.

Figure 7–video 1. 360° rotation video of in vivo streamlines.

327 vivo anatomical MRI that was even higher resolution. We showed that functional MRI is useful to
328 localize structures throughout the auditory pathway despite their small size. In each participant we
329 identified voxels significantly responding to sound presentation in regions corresponding to the CN,
330 SOC, IC and MGB. We validated these definition by evaluating both the within-subject reproducibility
331 (i.e., by comparing functional maps across two experiments in six individuals) and the ability of a
332 probabilistic atlas defined on nine out of our ten participants to generalize to the left out volunteer.
333   In total, we found that each of the methods described here provides information to the delin-
334 eation of the human subcortical auditory pathway. Our post mortem and in vivo data suggest that
335 MRI is a capable tool for investigating this system across spatial scales providing a bridge to the
336 gold standard, histology.
337   While not representing specific cells, MRI holds a number of advantages over the gold standard
338 method, histology (*Johnson et al., 1993*). First, MRI allows for visualization and analysis of an entire
339 3-D structure at once, with minimal geometric warping from (virtual) slice to slice (which can occur
340 in slice-based histology if individual slices contract on a slide or are damaged during the physical
341 slicing). Second, MRI can be used in vivo in human participants, opening up the possibility to
342 address research questions on the functional and anatomical properties of human subcortical
343 structures, their correspondence, and their involvement in human behavior.
344   Probing the connectivity of the human subcortical auditory pathway has been extremely limited,
345 since gold standard (but invasive) tracer studies are largely unavailable for human specimens. In
346 this study, we show that diffusion MRI tractography is sensitive to connections within the human
347 subcortical auditory system, both post mortem and in vivo. In addition to streamlines corresponding
348 to the lateral lemniscus-the major ascending auditory white matter tract-we can see streamlines
349 crossing the midline at the level of the superior olivary complex and the inferior colliculus.
350   Interestingly, with the highest resolution data (200 μm post mortem diffusion-weighted MRI),
351 we were able to estimate streamlines visually resembling the expected auditory pathway, but
352 missing putative key connections between subcortical auditory structures themselves when using
353 the strictly defined ROIs as tractography seeds. In contrast, the relatively lower resolution in vivo
354 diffusion-weighted MRI produced estimates of connectivity more like what we expected from the
355 literature. We had two hypotheses as to why these results appeared. First, the higher resolution
356 anatomical definition of the nuclei not including the immediately surrounding white matter could
357 miss streamlines that terminate at the immediate proximity of the structures' borders (similar
358 to issues in cortex (*Reveley et al., 2015*)). Second, partial volume effects in the lower resolution
359 data—combining white matter and grey matter in the same voxels—could actually *increase* stream-
360 lines terminating within the anatomical ROIs. Dilating the post mortem ROIs and downsampling the
361 data to the in vivo resolution both resulted in greater streamline connectivity between subcortical
362 auditory structures, suggesting that our hypotheses were likely. Thus, while high spatial resolution
363 diffusion-weighted MRI allowed for much finer, higher quality streamline estimates, it also places
364 constraints on tractography analyses that must be accounted for and investigated further.
365   More generally, the density of brainstem and midbrain nuclei and frequent crossings between
366 perpendicular white matter bundles pose a challenge to diffusion tractography estimations of white
367 matter connectivity, so it was not clear beforehand if this methodology would be sufficient for
368 visualizing these connections. Additionally, because a gold-standard connectivity method is not
369 available in humans, we could not directly validate our tractography findings (as can be done in the
370 macaque, though with limited success; see *Thomas et al.* (*2014*)). However, our results suggest that,
371 with continually improving diffusion-weighted MRI acquisition and analysis techniques, focused
372 investigations on the human subcortical auditory pathway can-and should-become more prominent
373 in the near future.
374   In addition to high resolution anatomical post mortem MRI and diffusion MRI tractography,
375 we were also able to identify the subcortical auditory system in vivo with functional MRI. Previous
376 studies have identified these structures with functional MRI, but they typically required constrained
377 acquisition parameters—for instance, they used single slices with low through-plane resolution

378 in order to support high in-plane resolution (*Guimaraes et al., 1998*; *Harms and Melcher, 2002*;
379 *Griffiths et al., 2001*; *Hawley et al., 2005*; *Sigalovsky and Melcher, 2006*). In the present study, by
380 taking advantage of the increased signal of high-field (7-Tesla) MRI, we were able to image the
381 brainstem using isotropic voxels at high resolution across a wider field-of-view that covers the
382 human auditory pathway in coronal oblique slices. The use of slice acceleration (*Moeller et al.,*
383 *2010*; *Setsompop et al., 2012*) allowed us to acquire enough slices to cover the whole brainstem,
384 thalamus and cortical regions around Heschl's gyrus with the exclusion of anterior portions of the
385 superior temporal gyrus and sulcus. Using isotropic voxels allowed us to better evaluate the 3-D
386 volume of significantly activated regions, limiting partial volume effects that are inevitable when
387 using thick anisotropic slices.

388 Similar to previous research at lower magnetic fields (*Hawley et al., 2005*; *Sigalovsky and*
389 *Melcher, 2006*), the 7T MR images did not allow for an anatomical definition of the CN and SOC
390 (although IC and MGB were clearly visible). A possible reason for this is the reduced signal- and
391 contrast-to-noise ratio in these regions. It should be noted that we could identify the SOC in the
392 MNI ICBM 152 dataset that results from the average of a much larger cohort. Therefore, future
393 investigations should be tailored to optimize anatomical image contrasts to auditory brainstem
394 regions in single subjects. The (post mortem) atlases we provide here will prove a useful tool for
395 these investigations by providing a reference for the expected location (and size) of these regions.

396 In contrast to in vivo anatomical localization, our data—in agreement with previous reports
397 (*Hawley et al., 2005*; *Sigalovsky and Melcher, 2006*)—show that *functional* mapping of the subcor-
398 tical auditory pathway is an effective method for localizing these structures. While histologically
399 defined CN and SOC regions have been previously used to sample functional responses from in vivo
400 fMRI data (*Hawley et al., 2005*; *Sigalovsky and Melcher, 2006*), the overlap between functionally
401 and histologically defined subcortical auditory structures has not been reported before. Here
402 we investigated the ability of BOLD fMRI (as an indirect measure of neuronal activity) to localize
403 subcortical auditory regions. We show that functional definitions are possible, as distinct clusters
404 of activation were detected in all subjects across the subcortical auditory pathway. These regions
405 were reproducible both within subjects (across experiments) and across subjects (comparing single
406 participants functional maps to the leave-one-out atlas obtained with all other participants). We
407 could identify the subcortical auditory nuclei despite not using cardiac gating, a method that previ-
408 ous studies showed to increase the signal-to-noise ratio in subcortical regions (*Guimaraes et al.,*
409 *1998*; *Harms and Melcher, 2002*; *Griffiths et al., 2001*; *Hawley et al., 2005*; *Sigalovsky and Melcher,*
410 *2006*). We instead increased statistical power by presenting a large number of natural sounds
411 with multiple repetitions. Using smaller voxels also reduced partial volume effects between cere-
412 brospinal fluid (which is heavily affected by physiological noise) and the brain tissue (*Triantafyllou*
413 *et al., 2016*). In addition, the correspondence of functionally defined regions across ten participants
414 after anatomical alignment allowed us to build a functional probabilistic atlas.

415 Despite these positive outcomes, functionally defined regions exhibited overall larger volumes
416 compared to the histological ones (see Table 1 in Fig 3). Although we acquired data at relatively
417 high resolution (1.1 mm isotropic), our functional voxel size and the mild spatial smoothing (1.5mm)
418 might be the source of this observation. Another factor that may have impacted the increased
419 volume of the in vivo probabilistic regions can be the residual anatomical misalignment across
420 subjects that also contributes especially to the lower degree of overlap at CN and SOC. In this case,
421 the individual anatomical images not showing enough contrast might be the cause. Partial volume
422 also most likely impacted small regions such as the CN and SOC, and draining effects due to the
423 vascular architecture could also have an impact on the size and localization of the in vivo defined
424 regions. Further, because we used only the overall response to sounds as functional definition, the
425 regions we defined may include sub-regions not specific to the system under investigation (e.g., the
426 inclusion of multisensory deep layers of the superior colliculus at the border with the IC) (*Sparks*
427 *and Hartwich-Young, 1989*; *Jiang et al., 1997*). This effect could be reduced by using different
428 stimuli and statistical contrasts. For instance, one could contrast uni-sensory and multi-sensory

stimuli to identify—within the current functional definition—the IC voxels that respond to visual stimulation and thus may represent multi-sensory superior colliculus. For the IC and MGB, where signal-to-noise ratio in the functional data is larger, a higher threshold in the probabilistic maps results in a more accurate volumetric definition as well as more correct anatomical localization (see, e.g., Fig. 6). It should also be noted that direct comparison of post-mortem and in vivo results suffers from the additional problem of aligning data with very diverse contrasts and resolutions. For the IC and MGB our procedure could be verified on the basis of the anatomical contrast in the in vivo data, for the CN and SOC the lack of anatomical contrast (to be leveraged by the alignment procedure) in the in vivo data may be the source of some of the misalignment between the data.

We also investigated the possibility of defining anatomical connections between subcortical auditory nuclei using diffusion-weighted MRI. While affected by similar confounds as functional MRI (e.g., partial voluming effects, physiological noise, and relative signal weighting), this technique faces additional complications introduced by the number of orientations required, the gradient strength (b-value) selected, the modeling of diffusion or fiber orientations within each voxel, and the estimation of streamlines across brain regions. The post mortem and in vivo diffusion MRI datasets in this study each implemented state-of-the-art acquisition techniques to optimize the MRI signal-to-noise ratio and minimize MRI modeling errors. For example, as the fixation process likely changes the diffusion characteristics of the tissue (*Pfefferbaum et al., 2004*; *Miller et al., 2011*), we compensated for this effect by increasing the diffusion gradient strength (b-value). The constrained spherical deconvolution modeling method takes advantage of the high angular resolution of each dataset to provide fine-grained estimations of fiber orientation distributions. Additionally, the Euler Delta Crossings (EuDX) deterministic tractography method is effective at generating streamlines through voxels with multiple fiber orientation peaks, such as where white matter bundles cross. However, as diffusion MRI and tractography are not measuring true neuronal connections, there is still room for error in diffusion orientation and streamline estimation (*Schilling et al., 2019a*,b).

Our BigBrain histological segmentations are very similar in volume to those reported previously in the literature (*Moore, 1987*; *Glendenning and Masterton, 1998*), with slightly smaller cochlear nuclei and slightly larger medial geniculate bodies, but similar SOC and IC volumes. It has to be noted that the physical slicing process potentially introduces deformations in the tissue, and while the publicly available BigBrain dataset is of extremely high quality (with good registration from slice to slice), subtle deformations may have affected the shape or volume of the structures we identified.

Post mortem MRI segmentations differed more greatly, with smaller CN and SOC definitions but larger MGB definitions compared to both the literature and BigBrain histological segmentations. These differences could possibly be caused by the reduced contrast-to-noise ratio in the post mortem MRI data compared to the histological data (despite their high spatial resolution). This reduced contrast-to-noise ratio may be caused by both reduced differences in magnetic properties between the regions and their surrounding tissues as well as from residual partial volume effects (especially for the very small sections of the dorsal CN, for example) that may have blurred the borders of the auditory nuclei in the post mortem MRI data. Contrast-to-noise ratio may be ameliorated by different acquisition/reconstruction techniques (*Wang et al., 2018*), and optimizing parameters may improve the definition of auditory nuclei on the basis of post mortem MRI data. Finally, slight misregistration between specimens (e.g. the histological data and the post mortem MRI data) likely still affect our comparisons, as registration between images (particularly from different modalities) remains a challenge. For instance, Fig. 2 shows slightly different shapes and locations for the inferior colliculus between the two datasets, despite non-linear registration to the same template. Although non-linear methods significantly improve gross registration between specimens, large misregistrations are still possible (as shown for the colliculi in the original BigBrain MNI registration). These issues can be addressed manually using additional image registration techniques, as we did here with the BigBrain MNI registration (see our "corrected" version above), but such hands-on, time-intensive edits are not always possible. Further, vastly different image

contrasts (like histology and MRI) result in different regions or subregions being emphasized in the signal, creating an additional challenges in the registration procedure.

More generally, post mortem imaging—whether MRI or histology—is prone to modest deformation of the specimen. Additionally, both post mortem specimens in this paper (BigBrain and post mortem MRI) were from 65-year-old male donors, and age may have additionally affected the volume of the brain structures we investigated.

Despite these limitations, the inter-rater and inter-experiment reliability in this study suggest that each method is effective for localizing the subcortical auditory pathway. The reliable functional localization of subcortical auditory structures opens the door to future investigations of more complex human auditory processing. The atlases derived from each localization method is publicly available (see "Data and code availability" in Methods) to facilitate further investigations into the structure, function, and connectivity of the human subcortical auditory system in vivo. Lastly, the 3-D representations found in this paper and in the available data should be beneficial to others in understanding the immensely complex, but identifiable, structure of the human subcortical auditory pathway.

Methods

See Supplementary Figure 3 for a summary of data sources, data processing steps, and software used in these analyses.

MRI acquisition parameters

In vivo MRI

The experimental procedures were approved by the ethics committee of the Faculty for Psychology and Neuroscience at Maastricht University, and were performed in accordance with the approved guidelines and the Declaration of Helsinki. Written informed consent was obtained for every participant before conducting the experiments. All participants reported to have normal hearing, had no history of hearing disorder/impairments or neurological disease.

Images were acquired on a 7T Siemens MAGNETOM scanner (Siemens Medical Solutions, Erlangen, Germany), with 70 mT/m gradients and a head RF coil (Nova Medical, Wilmington, MA, USA; single transmit, 32 receive channels) at Maastricht University, Maastricht, Netherlands.

We conducted two separate experiments. In Experiment 1, data were collected for n=10 participants (age range 25 to 30, 6 females), in three separate sessions. In the first session, we acquired the in vivo anatomical data set consisting of: 1) a T1-weighted (T1w) image acquired using a 3-D MPRAGE sequence (repetition time [TR] = 3100 ms; time to inversion [TI] = 1500 ms [adiabatic non-selective inversion pulse]; echo time [TE] = 2.42 ms; flip angle = 5°; generalized auto-calibrating partially parallel acquisitions [GRAPPA] = 3 (*Griswold et al., 2002*); field of view [FOV] = 224 × 224 mm^2; matrix size = 320 × 320; 256 slices; 0.7 mm isotropic voxels; pixel bandwidth = 182 Hz/pixel; first phase encode direction anterior to posterior; second phase encode direction superior to inferior); 2) a Proton Density weighted (PDw) image (0.7 mm iso.) with the same 3-D MPRAGE as for the T1w image but without the inversion pulse (TR = 1380 ms; TE = 2.42 ms; flip angle = 5°; GRAPPA = 3; FOV = 224 × 224 mm^2; matrix size = 320 × 320; 256 slices; 0.7 mm iso. voxels; pixel bandwidth = 182 Hz/pixel; first phase encode direction anterior to posterior; second phase encode direction superior to inferior); 3) a T2*-weighted (T2w) anatomical image acquired using a modified 3-D MPRAGE sequence (*De Martino et al., 2015*) that allows freely setting the TE (TR = 4910 ms; TE = 16 ms; flip angle = 5°; GRAPPA = 3; FOV = 224 × 224 mm^2; matrix size = 320 × 320; 256 slices; 0.7 mm iso. voxels; pixel bandwidth = 473 Hz/pixel; first phase encode direction anterior to posterior; second phase encode superior to inferior) and 4) a T1-weighted images acquired with a short inversion time (SI-T1w) using a 3-D MPRAGE (*Tourdias et al., 2014*) (TR = 4500 ms; TI = 670 ms [adiabatic non-selective inversion pulse]; TE = 3.37 ms; flip angle = 4°; GRAPPA = 3; FOV = 224 × 224 mm^2; matrix size = 320 × 320; 256 slices; 0.7 mm isotropic voxels; pixel bandwidth = 178

528 Hz/pixel; first phase encode direction anterior to posterior; second phase encode direction superior
529 to inferior). To improve transmit efficiency in temporal areas when acquiring these anatomical
530 images we used dielectric pads (*Teeuwisse et al., 2012*).

531 In the same session we acquired, for each participant, a diffusion-weighted MRI data set using a
532 multi-band diffusion-weighted spin-echo EPI protocol originating from the 7T Human Connectome
533 Project (1.05 mm isotropic acquisition and b-values = 1000 and 2000 s/mm^2) (*Vu et al., 2015*),
534 extended in order to collect one additional shell at b-value at b = 3000 s/mm^2 (*Gulban et al.,*
535 *2018a*). Other relevant imaging parameters were (FOV = 200 × 200 mm^2 with partial Fourier 6/8,
536 132 slices, nominal voxel size = 1.05 mm isotropic, TR/TE = 7080/75.6 ms, MB = 2, phase encoding
537 acceleration (GRAPPA) = 3, 66 directions and 11 additional b = 0 volumes for every b-value). A
538 total of 462 volumes were obtained (231 in each phase encoding direction anterior-posterior and
539 posterior-anterior) for a total acquisition time of 60 minutes.

540 The other two sessions were used to collect functional data in order to identify sound responsive
541 regions in the human thalamus and brainstem. Participants listened to 168 natural sounds (1
542 second long) coming from seven categories (speech, voice, nature, tools, music, animals and
543 monkey calls) presented in silent gaps in between the acquisition of functional volumes and were
544 asked to press a button every time the same sound was repeated. The experimental paradigm
545 followed a rapid-event-related design in which sounds were presented with a mean inter stimulus
546 interval of four volumes (minimum three maximum five volumes). The two sessions were identical
547 and each session consisted of twelve functional runs and across the twelve runs each sound was
548 presented three times (i.e. each sounds was presented six times across the two sessions). The 168
549 sounds were divided in four sets of 42 sounds, each set was presented in three (non consecutive)
550 runs. As a result, the twelve functional runs of each session formed four cross validation sets each
551 one consisting of nine training runs and three testing runs (i.e. 126 training and 42 testing sounds).
552 Note that the testing runs were non overlapping across the cross validations. Catch trials (i.e. sound
553 repetitions) were added to each run, and were excluded from all analyses.

554 Functional MRI data were acquired with a 2-D Multi-Band Echo Planar Imaging (2D-MBEPI)
555 sequence (*Moeller et al., 2010*; *Setsompop et al., 2012*) with slices prescribed in a coronal oblique
556 orientation in order to cover the entire brainstem and thalamus and covering primary and secondary
557 cortical regions (TR = 2600 ms; Gap = 1400 ms ; TE = 20 ms; flip angle = 80°; GRAPPA = 3; Multi-Band
558 factor = 2; FOV = 206 × 206 mm^2; matrix size = 188 × 188; 46 slices; 1.1 mm isotropic voxels; phase
559 encode direction inferior to superior). Reverses phase encode polarity acquisitions were used for
560 distortion correction. Respiration and cardiac information were collected during acquisition using a
561 respiration belt and pulse oximeter respectively.

562 In experiment 2, six of the volunteers that participated in experiment 1 were recalled and
563 functional data were acquired with the same slice prescription and functional MRI parameters as in
564 experiment 1 (2D-MBEPI; TR = 2600 ms; Gap = 1400 ms ; TE = 20 ms; flip angle = 80°; GRAPPA = 3;
565 Multi-Band factor = 2; FOV = 206 × 206 mm^2; matrix size = 188 × 188; 46 slices; 1.1 mm isotropic
566 voxels; phase encode direction inferior to superior). Experiment 2 consisted of two sessions
567 in which participants listened to 96 natural sounds (1 second long) coming from six categories
568 (speech, voice, nature, tools, music, animals) together with ripples (bandwidth = 1 octave; center
569 frequency = [300 Hz, 4 kHz]; AM rate = [3 Hz, 10 Hz]). Some ripple sounds contain a short noise
570 burst ('target') and participants were asked to detect such target in either low frequency ripples
571 or high frequency ripples in the two sessions respectively (the target occurrence varied (70 vs. 30
572 percent) for ripples whose center frequency did or did not match the current attention condition).
573 All sounds were presented in silent gaps in between the acquisition of functional volumes. The
574 experimental paradigm followed a rapid-event-related design in which sounds were presented
575 with a mean inter stimulus interval of four volumes (minimum three maximum five volumes). The
576 two sessions consisted of eight functional runs and across the eight runs each natural sound was
577 presented three times (i.e. each sounds was presented six times across the two sessions) while the
578 ripples were presented seven times per run. The 96 natural sounds were divided in four sets of

579 24 sounds, each set was presented in two (non consecutive) runs. As a result, the eight functional
580 runs of each session formed four cross validation sets each one consisting of six training runs
581 and two testing runs (i.e. 72 training natural sounds and 24 testing natural sounds). Note that
582 the testing runs were non overlapping across the cross validations. In each session of experiment
583 two we also collected a lower resolution (1 mm isotropic) anatomical reference images (T1 and PD
584 weighted) using the 3D MPRAGE sequence for alignment purposes and included reverses phase
585 encode polarity acquisitions for distortion correction. Respiration and cardiac information were
586 collected during acquisition using a respiration belt and pulse oximeter respectively.

587 Both in-vivo datasets acquired for experiment 1 and experiment 2 have never been published
588 before. This is the first work that uses this dataset.

589 Post mortem MRI

590 A human brainstem and thalamus specimen were dissected at autopsy from a 65-year-old anony-
591 mous male. The specimen was flushed with saline and immersed for two weeks in 10% solution of
592 neutral buffered formalin. Following this, the specimen was re-hydrated for one week in 0.1 M solu-
593 tion of phosphate buffered saline doped with 1% (5 mM) gadoteridol. Before the MRI acquisition,
594 the specimen was placed in custom MRI-compatible tube immersed in liquid fluorocarbon.

595 Magnetic resonance imaging was conducted in a 210 mm small-bore Magnex/Agilent MRI at the
596 Duke University Center for In Vivo Microscopy. 3-D gradient echo images were collected at 50 μm^3
597 spatial resolution over a period of fourteen hours, with FOV = 80 × 55 × 45 mm, repetition time (TR)
598 = 50 ms, echo time (TE) = 10 ms, flip angle = 60°, and bandwidth = 78 Hz/pixel.

599 Diffusion-weighted spin echo images were collected at 200 μm^3 spatial resolution with 120
600 diffusion gradient directions at strength b=4000 s/m^2 and 11 b=0 s/m^2 volumes over 208 hours.
601 The FOV was 90 × 55 × 45 mm with TR = 100 ms, TE = 33.6 ms, and bandwidth = 278 Hz/pixel.

602 **Anatomical image registration**

603 SI-T1w, T1w, T2*w and PDw images (700 μm iso.) were transformed to Talairach space (500 μm
604 iso.) using BrainvoyagerQX version 2.8.4 (*Goebel, 2012*). Intensity inhomogeneity correction as
605 implemented in SPM12 unified segmentation (*Ashburner and Friston, 2005*) was used for all images.
606 A smaller volume containing brainstem and thalamus in each image was extracted (in the Talairach
607 space) using FSL version 5.0.9 (*Jenkinson et al., 2012*) and histogram matched using percentile
608 clipping (1% and 99%).

609 Individual masks for each 10 brainstems were created semi-automatically using ITK-SNAP
610 version 3.6.0 active contour segmentation mode followed by manual edits. These masks included
611 regions starting from 2 cm below the inferior part of pons to 0.5 cm above the medial geniculate
612 nucleus (MGN), with a lateral extend reaching until the lateral geniculate nucleus (LGN) and 3 cm
613 anterior from MGN, not including cerebellum or large arteries that lie on the surface of brainstem.
614 These brainstem masks were then used with FSL-FNIRT (*Andersson et al., 2007*) to warp nine of
615 the ten brainstems to the reference brainstem (subject 1) using SI-T1w images. We used the SI-
616 T1w images to drive the non linear registration due to the enhanced anatomical contrast across
617 structures within the thalamus and brainstem present in these images (*Tourdias et al., 2014*;
618 *Moerel et al., 2015*). The FNIRT parameters were subsamp = 2, 2, 1, 1, miter = 100, 100, 50, 50,
619 infwhm = 2, 2, 1, 1, reffwhm = 2, 2, 0, 0, lambda = 100, 50, 20, 5, estint = 0, 0, 0, 0, warpres = 2, 2, 2 with
620 spline interpolation (parameters not mentioned here were the defaults as set in FSL 5.0.9).

621 To compare in vivo with post mortem MRI and histology data, we projected the averaged SI-T1w,
622 T1w, T2*w and PDw images to the MNI reference space (ICBM 152 2009b non-linear symmetric,
623 500 μm iso.) (*Fonov et al., 2009*, *2011*) [1]. The ICBM 152 reference includes T1w, T2w and PDw data
624 and projecting in vivo and post mortem MRI as well as histology data to this space allowed us also
625 to evaluate the contrast that these commonly used template images have in subcortical auditory

[1]http://www.bic.mni.mcgill.ca/ServicesAtlases/ICBM152NLin2009

626 areas. To register our in vivo MRI data set to MNI, we used FSL-FNIRT but this time driven by the
627 T1w images (available both in our data set and in the MNI ICBM 152 2009b data).

628   The post mortem diffusion b0 image was transformed to the post mortem anatomical image
629 space with an affine transformation in ANTs. Anatomical-space images (including the manually
630 segmented atlas) could then be transformed into diffusion space using the 'antsApplyTransforms'
631 command, with the affine transform matrix, a super-sampled diffusion image (from 200 μm to 50
632 μm to match the anatomical image resolution) as the reference image, and denoting the warp as
633 an inverse transform.

634   In vivo and post mortem images were registered non-linearly using ANTs. The in vivo SI-T1w
635 image was warped to the post mortem diffusion b0 image following a rigid, then affine, then
636 non-linear SyN algorithm. This produced an in vivo brainstem image in post mortem diffusion
637 space.

638   The ANTs non-linear registration also created warp and inverse warp transforms that could then
639 be used to transform atlases from one space to another. To preserve the higher resolution of the
640 post mortem MRI when inverse warping post mortem images to in vivo space, we supersampled
641 the in vivo SI-T1w image to 200 μm (matching the post mortem diffusion image) or 50 μm (matching
642 the post mortem anatomical image).

643   Finally, to transform the post mortem anatomical image (50 μm) to MNI space, we applied the
644 inverse transform from post mortem anatomical to diffusion space (resampled to 50 μm), then the
645 inverse transform from diffusion space to in vivo space (similarly upsampled to 50 μm), and finally
646 from in vivo space to MNI space using the FSL-FNIRT inverse transform (described above).

647 **BigBrain histology segmentation**

648 In what follows we describe the main anatomical observations related to the auditory structures
649 as segmented in the 100 μm histological data. Images were segmented independently by two
650 raters (KRS, OFG). Overlap between the two raters was high (see Table 2 [top row - Big Brain across
651 segmenters] in Fig 2); in the figures we show the regions that were consistently segmented by both
652 raters.

653 Vestibulocochlear nerve

654 The vestibulocochlear nerve (the eighth cranial nerve, or CNVIII) enters the brainstem where
655 the medulla and the pons meet (the pontomedullary junction). The cochlear component of the
656 vestibulocochlear nerve is composed of spiral ganglion neurons, whose cell bodies are within the
657 cochlea and which carry frequency-specific information to the brainstem.

658   In the BigBrain histology, CNVIII extends primarily laterally (but also anteriorly and inferiorly)
659 from the pontomedullary junction, bound posteriorly by the cerebellum. Parts of the nerve root are
660 still visible in the images although being cut. It is therefore not labeled in our histological atlas (but
661 see the post mortem MRI atlas below).

662 Cochlear nucleus

663 Once reaching the brainstem, the auditory nerves split into two main routes-one to the anterior
664 ventral cochlear nucleus (AVCN), and one to the posterior ventral cochlear nucleus (PVCN) and then
665 on to the dorsal cochlear nucleus (DCN) (*Webster, 1992*). Within each subnucleus, the neurons
666 maintain the tonotopic frequency representation they receive from the cochlea via the cochlear
667 nerve (*De No, 1933b*,*a*; *Rose et al., 1960*; *Sando, 1965*; *Evans, 1975*; *Ryugo and May, 1993*; *Ryugo
668 and Parks, 2003*) (see bottom panels of the two left most columns in Fig 2).

669   In the BigBrain data, the AVCN is situated anterior and medial to the root of CNVIII, while the
670 PVCN continues from the root of CNVIII and extends posteriorly towards the DCN. The DCN is clearly
671 visible as a dark band wrapping around the cerebellar peduncle posteriorly, becoming exposed on
672 the dorsal surface of the pons.

Manuscript submitted to eLife

Superior olivary complex

The next structure along the auditory pathway is the superior olivary complex (SOC), which in humans is located in the inferior pons. The SOC receives the majority of its ascending inputs from the contralateral cochlear nucleus, although it also receives ipsilateral inputs as well. The contralateral dominance is maintained throughout the remaining ascending pathway. The SOC is comprised of the lateral superior olive (LSO), medial superior olive (MSO), and the medial nucleus of the trapezoid body (MNTB). The size of each of these nuclei varies between species, and it is debated whether the trapezoid body exists in the human SOC (*Moore, 1987*; *Strominger and Hurwitz, 1976*) (but see *Kulesza and Grothe* (*2015*) review of recent findings affirming the existence of the human MNTB).

Although the individual substructures within the SOC have unique anatomy that can be identified from histology (*Moore, 1987*; *Kulesza, 2007*), here we outline the structure of the SOC as a whole in order to include all identifiable substructures (namely the MSO and LSO - see second panel from the bottom of the two left most columns in Fig 1). The MSO is the largest SOC nucleus in humans, unlike in other animals. The MSO receives inputs from both the left and right AVCN and sends outputs to the ipsilateral lateral lemniscus. The LSO receives inputs from the ipsilateral AVCN and from the ipsilateral MNTB. Outputs are sent to both ipsilateral and contralateral lateral lemnisci. The MNTB receives inputs from the contralateral AVCN, and its axons terminate in the ipsilateral LSO.

The MSO and LSO are visible in the BigBrain images, despite their small size. The MSO is a thin pencil-like collection of nuclei whose caudalmost point begins around the same axial plane as the rostralmost extent of the AVCN, about 4 mm medial (and slightly anterior) to the AVCN. It then extends about 1 cm rostrally (angled slightly laterally), where it eventually meets the lateral lemniscal tract. The LSO neighbors the MSO near its caudalmost portion, forming a "V" shape when viewed axially. In our histological atlas, these two structures are combined into a single SOC segmentation. Cells of the MNTB are not clear to us in this sample, so we do not segment it in our atlas.

Inferior colliculus

The inferior colliculus (IC) is a large, spherical structure in the dorsal midbrain and receives ascending inputs from the auditory brainstem via the lateral lemniscus (see second panel from the top of the two left most columns in Fig 1). The central nucleus of the inferior colliculus receives most of these connections, with external nuclei primarily receiving descending connections (*Webster, 1992*). The inferior colliculus sends axons to the medial geniculate body of the thalamus via the brachium of the inferior colliculus.

In the BigBrain data, the inferior colliculus is clearly identifiable as the lower two of the four bumps along the dorsal portion of the midbrain (or tectum). The darkest staining within these structures corresponds to the central nucleus of the inferior colliculus. An intensity gradient outside of the central nucleus likely corresponds to the external and dorsal nuclei, which were included in our segmentation of the IC. Bounding the IC superiorly is the superior colliculus; medially, the commissure of the IC connecting the two inferior colliculi, as well as the aqueduct and periaqueductal grey; and anteriorly, other midbrain nuclei such as the cuneiform nucleus (lateral and inferior to the IC are the borders of the midbrain).

Medial geniculate of the thalamus

The medial geniculate body (MGB) of the thalamus is the final subcortical auditory structure that sends auditory signals to the auditory cortex via the acoustic radiations (*Winer, 1984*) (see top panel of the two left most columns in Fig 1). The MGB contains two or three major subdivisions: the ventral MGB receives the majority of IC inputs, while the dorsal and medial subdivisions (at times grouped together, at times separately) receive more varied inputs from auditory and non-auditory subcortical structures.

722   In the BigBrain sample, the MGB is visible as a dark patch medial to the lateral geniculate nucleus
723 (which can be easily identified by its striations) in a coronal view. Axially, the MGB takes an ovoid
724 shape with a clear dorsolateral boundary next to the brachium of the superior colliculus, which
725 appears light due to lack of cell nuclei being stained. Ventromedially, the MGB is bordered by a light
726 band corresponding to the medial lemniscus. Rostrally, we marked the edge of the MGB where cell
727 staining decreases, at the border with the pulvinar nucleus and ventral posterolateral nucleus of
728 the thalamus.

729 **Post mortem MRI segmentation**
730 In what follows we describe the anatomical contrast that can be leveraged from these post mortem
731 MRI data in order to identify structures in the auditory brainstem. We then used these segmenta-
732 tions to create an MRI-based atlas of the subcortical auditory system, separate from the BigBrain
733 histology-based atlas.

734 Vestibulocochlear nerve
735 The CNVIII is visible in the post mortem MRI near the pontomedullary junction, extending laterally
736 and anteriorly from the brainstem (see the lower panels in Fig 2).

737 Cochlear nucleus
738 The cochlear nuclei are challenging to identify in the post mortem MRI data, although the presence
739 of the CNVIII root provides a landmark for localizing the other structures. Due to low signal contrast
740 around the ventral cochlear nucleus area in the T2*-weighted GRE MRI, we segmented the VCN
741 according to the literature: bound by the cochlear nerve root and wall of the pons laterally, and
742 by cerebellar white matter tracks medially. We were able to segment the dorsal cochlear nucleus
743 based on the T2*-weighted image, where it appears brighter and can be identified as running
744 posteriorly from the VCN and dorsally along the surface of the pons, distal to the inferior cerebellar
745 peduncle.

746 Superior olivary complex
747 As with the cochlear nuclei, the SOC are more difficult to identify in the post mortem MRI than in the
748 histology, likely since the individual subnuclei like the MSO and LSO approach the size of a voxel in
749 at least one direction and are therefore prone to partial voluming effects. However, the pencil-like
750 MSO can still be identified in the coronal plane as a dark, elongated structure in the T2*-weighted
751 image, starting around the level of the ventral cochlear nucleus. In the axial plane, the SOC (but not
752 its individual subnuclei) can be seen as a dark spot in the T2*-weighted image between the facial
753 nucleus and the trapezoid body (see the second row from the bottom in Fig 2).

754 Inferior colliculus
755 As in the BigBrain data, the inferior colliculus is relatively easy to identify based on its gross
756 anatomical structure on the dorsal aspect of the midbrain. Additionally, the MR contrast provides
757 relatively clear boundaries between the colliculi and surrounding structures. Indeed, it may even be
758 possible to segment the inferior colliculus into its subnuclei-the central, external, and dorsal nuclei-
759 based on T2*-weighted MR signal intensities (see the second row from the top in Fig 2). The external
760 nucleus of the IC appears dark in the T2*-weighted image, on the lateral aspect of the IC. Medial
761 to the external nucleus is the central nucleus, which has higher T2*-weighted intensity (appears
762 brighter) in our MR images, and has clear boundaries on its ventral, medial, and dorsolateral sides.
763 The dorsal nucleus is along the dorsal aspect of the IC and is the brightest subcomponent within
764 the IC in terms of T2*-weighted MR signal.

765 Medial geniculate
766 Although the borders of the MGB are less clear in the post mortem MRI than in the BigBrain images,
767 the structure itself is again relatively easy to identify by its gross anatomical location as well as

768 MR signal intensity. In the coronal plane, the medial geniculate is medial to the lateral geniculate
769 at the junction of the midbrain and thalamus. Axially, the medial geniculate has circular or ovoid
770 shape, again medial to the lateral geniculate. In the axial plane, the medial geniculate is largely
771 bordered dorsolaterally by the brachium of the superior colliculus, which appears as a thick, dark
772 band of fibers in the T2*-weighted image. Medially, the medial geniculate is bound by the brachium
773 of the inferior colliculus (also appearing as a dark fiber band), at least through the caudal half
774 of the structure. We have included the portions of this fiber bundle in the segmentation of the
775 medial geniculate, as the auditory fibers connecting the IC and the MGB are quite relevant to MRI
776 connectivity investigations (including our own; post mortem tractography results below).

777 As with the inferior colliculus, it may be possible to identify separate divisions within the medial
778 geniculate. Within the overall structure, there are two identifiable substructures based on T2*-
779 weighted MR image intensity. Dorsomedially (and somewhat caudally), about half of the medial
780 geniculate has high T2*-weighted contrast and appears bright; the ventrolateral (and slightly rostral)
781 half appears darker in the T2*-weighted image. These segmentations largely (but not perfectly)
782 align with the ventral and dorsal/medial nuclei of the medial geniculate in the Allen Human Brain
783 Atlas (*Hawrylycz et al., 2012*), as well as with those of *Paxinos et al.* (*2019*). However, they vary
784 somewhat from the the axial slice segmentation from *Merker* (*1983*) shown in *Amunts et al.* (*2012*),
785 which show a largely horizontal delineation between the substructures.

Functional MRI analysis

787 In both functional experiments, data were preprocessed using BrainvoyagerQX version 2.8.4
788 (*Goebel, 2012*). Slice-scan-time correction, motion correction, temporal high-pass filtering (GLM-
789 Fourier, 6 sines/cosines) and temporal smoothing (Gaussian, width of kernel 5.2 s). The defaults
790 in BrainvoyagerQX v2.8.4 were used for these steps aside from the explicitly stated values. The
791 functional images were then distortion corrected using the opposite phase encoding direction
792 images using FSL-TOPUP (*Andersson et al., 2003*). Conversion between Brainvoyager file types to
793 NIfTI which was required to perform distortion correction was done using Neuroelf version 1.1
794 (release candidate 2) [2] in Matlab version 2016a. For alignment across experiments (i.e. to co-register
795 the data of experiment 2 to the ones collected in experiment 1) we used FSL-FLIRT. In this procedure
796 the alignment between the functional data of the two experiments was tailored to a mask that
797 included the brainstem, thalamus and auditory cortex.

798 After pre-processing, functional images were then transformed to Talairach space using Brain-
799 voyager at a resolution of 0.5 mm isotropic. We have previously used this procedure in order to
800 reveal tonotopic maps in both the inferior colliculus and medial geniculate nucleus (*De Martino*
801 *et al., 2013*; *Moerel et al., 2015*) and have shown that the upsampling has no consequence on the
802 spatial distribution of the responses. Upsampling can also reduce effects of interpolation that
803 is common during resampling in many image processing steps. After upsampling, mild spatial
804 smoothing (Gaussian, FWHM 1.5mm) was also applied. Supplement figure 5 to Fig. 5 shows the
805 effect that spatial smoothing has on the activation maps obtained from two participants data in
806 experiment 1.

807 GLM-denoise (*Kay et al., 2013*) was used to estimate noise regressors. In brief, for each cross
808 validation a noise pool of non responsive voxels (i.e. voxels with a response to sound representation
809 determined by an F-statistic below a given threshold) was determined on the training data set (16
810 runs across the two sessions of experiment 1 and 12 runs across the two sessions of experiment 2)
811 and used to obtain noise regressors defined as the principal components of the noise pool time
812 course matrix that added to a GLM analysis (*Friston et al., 1994*) of the training data would result
813 in an increased activation. The number of noise regressors was optimized using cross validation
814 within the training set. The selected noise regressor spatial maps were projected on the test data to
815 obtain the regressors for the test data.

---

[2]http://neuroelf.net/

Manuscript submitted to eLife

Similarly, the hemodynamic response function (HRF) best characterizing the response of each voxel in the brainstem was obtained using a deconvolution GLM (with 9 stick predictors) on the training data. Note that this procedure, while possibly overfitting information in the training data, produces noise regressors and an HRF for each test run (e.g. the noise regressors for runs 4, 6 and 9 of session one in experiment 1 comes from an analysis performed on all other runs in the same session) that are not overfitted.

The resulting HRF and noise regressors were used in a GLM analysis of the test runs. We combined all test runs (for each individual voxel) using a fixed effect analysis.

Statistical maps of responses to sounds vs silence were corrected for multiple comparisons at the individual level using False Discovery Rate (FDR; q-FDR = 0.05). An additional threshold on the uncorrected p-value of each voxel (i.e. p<0.001) was applied to further reduce the number of false positive activation that can be expected when applying FDR. Unless otherwise stated, single subject statistical maps are displayed by color coding voxels that surpass these statistical thresholds. Unthresholded statistical maps are visualized in 10 and are available at the online repository of the data (https://osf.io/hxekn/?view_only=be9ec398304344e8bb694a0658d77ed6) for inspection.

The functional activation maps of the six participants that took part in both experiments have been analyzed to demonstrate within participant reproducibility of effects. Since the stimuli were different and the number of runs were different, this second experiment shows a generalization of the first experiment, thereby additionally validating the detection of these structures. Figure supplement 3 to Figure 5 shows the statistically thresholded activation maps for each of this six participants for the two experiments in three anatomical cuts (two transversal for CN/SOC and IC and one coronal for the MGB). The percentage of statistically significant voxels in experiment 1 that are statistically significant in experiment 2 is reported toegther with the distance between the centroids of activations between the two experments in supplementary supplement figure 4 to Figure 5 (for each individual and in average across individuals). The unthresholded maps of both experiments (for each of the six participants) are also visualized in Figure 11 and are available at the online repository (https://osf.io/hxekn/?view_only=be9ec398304344e8bb694a0658d77ed6) for inspection.

To produce group level results, the single subject statistical maps were warped to the reference brainstem (subject 1) by applying the warping field obtained on the anatomical data. After projection to the common space, single subject statistical maps were binarized and converted to a probabilistic map by: 1) applying of a cluster size threshold of 3.37 mm^3 (27 voxels in the 0.5 mm isotropic anatomical space 2.5 voxels in the original functional resolution) and 2) summing maps across subjects at each single voxel (i.e. a value of 10 indicates that all 10 subjects exhibited a statistically significant response to sound presentation corrected for multiple comparisons and belonging to a cluster of at least 27 voxels in the anatomical space). The additional clustering allowed us to further control for possible false positives by imposing a neuroanatomically plausible hypothesis (i.e. none of our region of interest is smaller than 3.37 mm^3 in volume). The same procedure was also repeated by leaving one subject out (i.e. we generated probabilistic maps from 9 out of the ten subjects each time leave one subject out). The leave one out probabilistic maps where then back projected to the anatomical space of the left out subject (i.e. the probabilistic map obtained from subjects 1 to 9 was back projected to the anatomical space of subject 10). Unless otherwise stated, probabilistic maps are displayed with minimum threshold of at least three out of ten (or nine for the leave one out maps) subjects exhibiting significant responses at each voxel. Unthresholded probabilistic maps are available for inspection at the online repository.

We evaluated how well cluster localized on the basis of our probabilistic maps generalize to new data. Figure 5 displays the statistically thresholded activation maps for each of the ten participants in experiment 1 in three anatomical cuts (two transversal for CN/SOC and IC and one coronal for the MGB) together with the probabilistic map obtained from the other nine participants (thresholded by displaying voxels that are functionally significant in at least three out of nince participants). In supplement figure 1 to figure 5 we report the percentage of voxels in the leave

one out probabilistic maps that are statistically significant in the left out subject. The overlap is reported toegther with the distance between the centroids of activations in the leave one out probabilistic maps and the left out subject. The effect of the threshold on the probabilistic maps is analyzed in supplement figure 2 to figure 5. The unthresholded maps (leave one subject out and single subject) are also visualized in figure 10 and available at the online repository (https://osf.io/hxekn/?view_only=be9ec398304344e8bb694a0658d77ed6) for inspection.

To compare the functional activation maps with histology data and post mortem MRI data, the probabilistic maps were projected to the MNI space using the warping field obtained from the anatomical dataset.

BigBrain data

Histology data were obtained by downloading the 100 µm version of the BigBrain (*Amunts et al., 2013*) 3-D Volume Data Release 2015 (from https://bigbrain.loris.ca). We downloaded both the original images and the dataset already aligned to MNI ICBM 152. The nuclei along the auditory pathway (cochlear nucleus, superior olive, inferior colliculus and medial geniculate nucleus) were manually segmented in the histology space image using ITK-SNAP (*Yushkevich et al., 2006*) largely following the definitions in *Moore* (*1987*) when possible.

Correction of the alignment of the inferior colliculi to MNI

Upon visual inspection of the BigBrain image in the MNI ICM 152 space, we detected a major registration error around the inferior colliculi (see Fig 8 - second panel from the left). The registration quality to MNI ICMBM 152 space in the rest of the brainstem was deemed satisfactory, but the the region of the inferior colliculus required correction in order to perform a valid comparison with the MRI data (in vivo and post mortem). Interestingly, the region of the colliculi of the BigBrain in the original histology space appeared to be closer in location to the position of the inferior colliculus in the MNI dataset (compare panel 1 and 3 in Fig 8) indicating that the highlighted misalignment in the original BigBrain MNI dataset originated during the registration procedure.

To perform a new registration to MNI of the brainstem and thalamus of the BigBrain data that observed the already correctly registered boundaries (e.g. the Pons) but corrected the region around the inferior colliculus bilaterally, we followed N steps. First, we defined a region of interest around the inferior colliculus using common anatomical landmarks that were visible in the BigBrain MNI and MNI (2009b) T1, PD, T2 images and where aligned satisfactorily. Second, this region was cut out from the BigBrain MNI and replaced by the same region (i.e. defined by the same anatomical landmarks) in the BigBrain histology space data (before projection to MNI). The convex hulls of the region of interest in the BigBrain histology and in the MNI space were matched using 3-D optimal transport as implemented in Geogram version 1.6.7 (*Lévy, 2015*; *Lévy and Schwindt, 2018*). Third, the convex hull matched region of the the BigBrain histology space was used to replace the incorrect region which was cut out at step 2. As a result of these three steps we obtained a version of the BigBrain in MNI (BigBrain MNI - implanted) that had the inferior colliculus in the right position but where the transitions between outside to inside of the region of interest that was corrected were visible and not respecting of the topology. To correct for these residual errors, we performed a new FSL-FNIRT alignment between the original BigBrain in histology space and the BigBrain MNI - implanted image. The resulting image (BigBrain MNI - corrected) preserved the actual topology inside the brainstem and at the same time resulted in a correct alignment of the regions around the inferior colliculus bilaterally (see Fig 8 - right panel).

Post mortem MRI vasculature analysis

Gradient echo (GRE) MRI is sensitive to vasculature within the imaged tissue. To highlight vasculature in the post mortem brainstem specimen, we computed the minimum intensity projection in coronal sagittal and axial direction from the 50 µm isotropic voxel GRE MRI data over slabs of 1.1 mm in

Manuscript submitted to eLife

BigBrain (100 μm)   BigBrain (100 μm)   MNI ICBM 152 (500 μm)   BigBrain (100 μm)
Histology space   MNI ICBM 152   2009b T1w   MNI ICBM 152 (corrected)
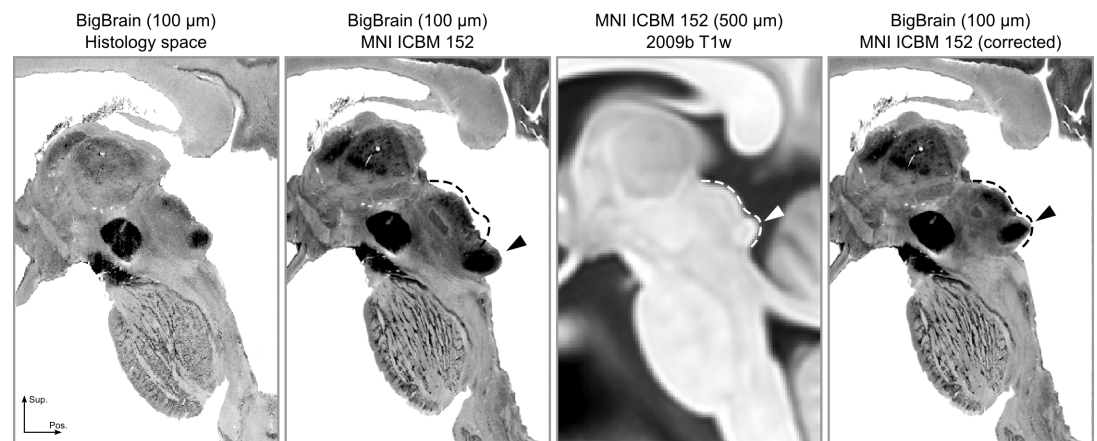
Figure 8. The registration error around the inferior colliculus is visible bilaterally when comparing Panel 2 and Panel 3. The dashed lines indicate the correct shape (and location) of the colliculi in MNI space. The arrows point to the inferior colliculus (IC). The last panel shows the corrected BigBrain MNI dataset.

914 thickness using Nibabel (*Brett et al., 2017*) and Numpy (*Van Der Walt et al., 2011*)). This image can
915 be seen in Fig 6 right column.

Diffusion MRI analysis

Post mortem diffusion

918 Before analysis, post mortem diffusion volumes were each registered to the first b0 volume using
919 an affine transformation in ANTs version 2.1.0 (*Avants et al., 2011*). To estimate white matter fiber
920 orientations, we used the constrained spherical deconvolution (CSD) model as implemented in DIPY
921 0.14 (*Gorgolewski et al., 2011*; *Garyfallidis et al., 2014*; *Tournier et al., 2007*) as a Nipype pipeline
922 (*Gorgolewski et al., 2011*). CSD posits that the observed diffusion signal is a convolution of the
923 true fiber orientation distribution (FOD) with a response function. DIPY's 'auto-response' function
924 estimates the fiber response function from a sphere of 10 voxels in the center of the sample above
925 a given fractional anisotropy (FA) threshold (0.5 in our study). We then estimated FOD peaks in
926 each voxel using DIPY's 'peaks-from-model' method with a 10° minimum separation angle and a
927 maximum of 5 peaks per voxel.

928 White matter fiber streamlines were estimated deterministically with DIPY's EudX method (*Mori*
929 *et al., 1999*; *Garyfallidis, 2013*) with 1,000,000 seeds per voxel, a 75° streamline angle threshold,
930 and an FA termination threshold of 0.001 (since data outside the specimen sample were already
931 masked to 0).

932 To define regions of interest (ROIs) for the fiber display, the auditory structures manually
933 delineated in the post mortem T2*-weighted MR images were transformed to diffusion space
934 using ANTs, and global streamlines were filtered by considering only the voxels in each one of the
935 ROIs as a seed and further constrained by using all auditory ROIs as tractography waypoints. This
936 resulted in a high-resolution, high-quality auditory-specific subcortical tractogram, which were then
937 visualized in TrackVis 0.6.1 (*Wang et al., 2007*).

In vivo diffusion

939 7T in vivo dMRI data was corrected for distortions with the HCP pipeline *Glasser et al.* (*2016*);
940 *Sotiropoulos et al.* (*2013*). Specifically, geometric and eddy-current distortions, as well as head
941 motion, were corrected by modeling and combining data acquired with opposite phase encoding
942 directions *Andersson et al.* (*2003*); *Andersson and Sotiropoulos* (*2015*, 2016). The data were then
943 masked to include just the brainstem and thalamus, matching the post mortem specimen.

944 Similar to the post mortem analysis, we estimated diffusion FODs with a CSD model imple-
945 mented in DIPY with response function FA threshold of 0.5. Peaks were extracted with a minimum

Manuscript submitted to eLife
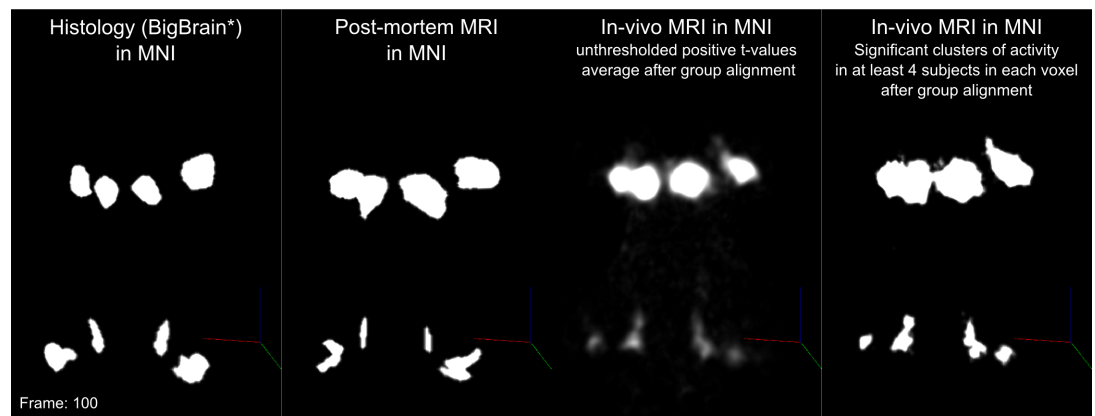
Figure 9. One frame of volume rendered animations for comparing histology (BigBrain), post-mortem MRI, in-vivo MRI unthresholded positive t-values group average and in-vivo MRI clusters of significant activity overlapping in at least 4 subjects in each voxel.

Figure 9–video 1. 3D volume rendered comparisons in MNI space.

separation angle of 25°. White matter connectivity was estimated with deterministic tractography throughout the brainstem and thalamus, again using DIPY's EudX algorithm (*Mori et al., 1999*; *Garyfallidis, 2013*) with 1,000,000 seeds per voxel, a 45° streamline angle threshold, and an FA termination threshold of 0.023.

For the tractography in the in vivo data we used subcortical auditory ROIs as defined by the analysis of the functional data (i.e. regions that exhibited significant [corrected for multiple comparisons] response to sound presentation in at least three out of ten subjects). The functional ROIs were transformed to individual diffusion space and used as tractography seeds, with all other auditory ROIs as waypoints, producing a subcortical auditory tractogram for each in vivo subject.

Data and code availability

Unprocessed in vivo data are available at (https://openneuro.org/datasets/ds001942). Atlas segmentations and tractography streamlines are available through the Open Science Framework (https://osf.io/hxekn/). Processing and analysis resources, including links to all data and software used in this paper, are available at https://github.com/sitek/subcortical-auditory-atlas. See Supplementary Figure 3 for an overview of currently available data and code (full resolution version available at our code repository).

Animated 3D volume renderings

Video animations in Figure 9, Figure 10 and Figure 11 were created using pyqtgraph (v0.10.0, http://www.pyqtgraph.org/) volume rendering. The t-value maps were clipped to 0-20 range and scaled to 0-255 range. These t-values are 3D volume rendered by assigning the corresponding gray value to each voxel as well as the alpha channel (transparency). Which means that lower values are closer to black and translucent. Animation frames were generated by rotating camera one degree at a time for 360 degrees. Additive rendering was used for 2D projections to provide depth vision (i.e. for preventing voxels closest to the camera from seeing values inside the clusters.).

Acknowledgements

Manuscript submitted to eLife
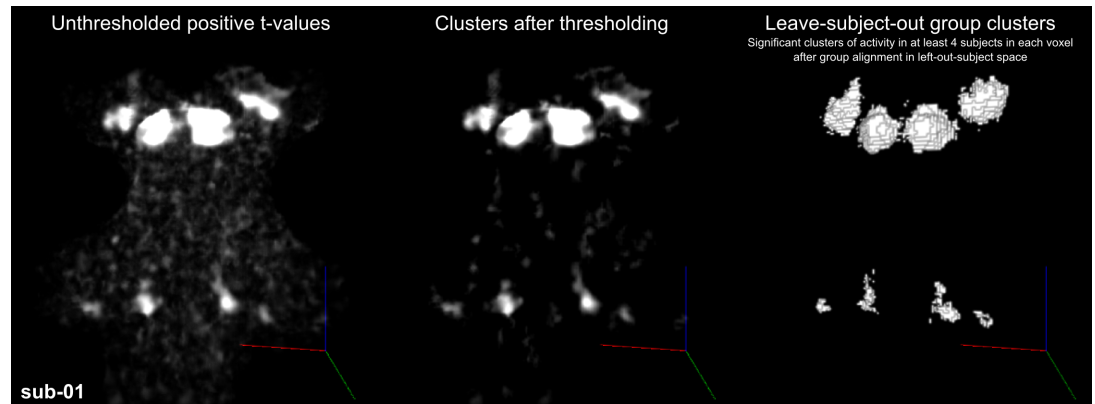
Figure 10. One frame of volume rendered animations for single subject statistical maps. (Left)positive t-values (middle) after thresholding (right) leave-one-out probabilistic map ($\geq$ 4)). Viewing angle here is similar to Figure 1.

Figure 10–video 1. Subject 01

Figure 10–video 2. Subject 02

Figure 10–video 3. Subject 03

Figure 10–video 4. Subject 05

Figure 10–video 5. Subject 06

Figure 10–video 6. Subject 07

Figure 10–video 7. Subject 08

Figure 10–video 8. Subject 09

Figure 10–video 9. Subject 10

Figure 10–video 10. Subject 11
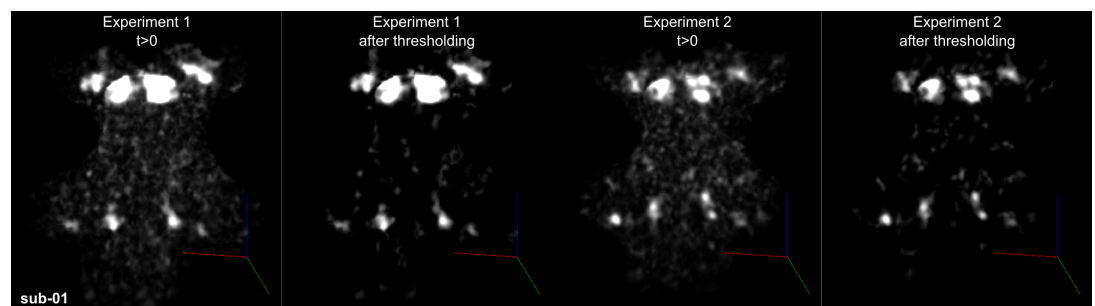
Figure 11. One frame of volume rendered animations for Subject 01 statistical maps (experiment 1 positive t-values & thresholded (col 1-2) and experiment 2 positive t-values & thresholded (col 3-4)). Viewing angle here is similar to Figure 1.

Figure 11–video 1. Subject 01 experiment 1 vs experiment 2.

Figure 11–video 2. Subject 02 experiment 1 vs experiment 2.

Figure 11–video 3. Subject 05 experiment 1 vs experiment 2.

Figure 11–video 4. Subject 09 experiment 1 vs experiment 2.

Figure 11–video 5. Subject 10 experiment 1 vs experiment 2.

Figure 11–video 6. Subject 11 experiment 1 vs experiment 2.

Figure 11–video 7. Group average (N=6) unthresholded positive t-values for experiment 1 vs experiment 2.

976 the Eaton Peabody Laboratory at Mass. Eye and Ear (Boston, MA, USA), and a travel grant from
977 the Harvard Brain Science Institute. MR Histology was acquired at the Duke Center for In Vivo
978 Microscopy, an NIH/NIBIB National Resource (P41EB015897 to G.A.J.), NIH 1S10OD010683-01 (to
979 G.A.J.).

Glossary
980

Anatomical abbreviations
981

AVCN	Anteroventral cochlear nucleus.
CN	Cochlear nucleus.
CNVIII	8th nerve, vestibulocochlear nerve.
DCN	Dorsal cochclear nucleus.
IC	Inferior colliculus.
LGN	Lateral geniculate nucleus.
LSO	Lateral superior olive.
MGB/MGN	Medial geniculate body/nucleus.
MNTB	Medial nucleus of the trapezoid body.
MSO	Medial superior olive.
PVCN	Posteroventral cochlear nucleus.
SOC	Superior olivary complex.

982

MRI acquisition abbreviations
983

7T	7 Tesla.
dMRI	diffusion magnetic resonance imaging.
FOV	Field of view.
fMRI	functional magnetic resonance imaging.
GRAPPA	Generalized auto-calibrating partially parallel acquisitions.
MB	Multi-band.
MPRAGE	Magnetization prepared rapid acquisition gradient echo.
MRI	Magnetic resonance imaging.
PDw	Proton density weighted.
SI-T1w	Short inversion time T1-weighted.
T1w	T1-weighted.
T2*w	T2*-weighted.
TE	Echo time.
TR	Repetition time.

984

Data analysis abbreviations

CSD	Constrained spherical deconvolution.
FA	Fractional anisotropy.
FDR	False discovery rate.
FOD	Fiber orientation distribution.
GLM	General linear model.
HCP	Human connectome project.
HRF	Hemodynamic response function.
ICBM	Internation Consortium for Brain Mapping.
M0	T2 signal with no diffusion weighting.
MD	Mean diffusivity.
MNI	Montreal Neurological Institude.
MSMT	Multi-shell multi-tissue
ODFs	Orientation distribution functions.
ROI	Region of interest.

References

Amunts K, Lepage C, Borgeat L, Mohlberg H, Dickscheid T, Rousseau MÉ, Bludau S, Bazin PL, Lewis LB, Oros-Peusquens AM, Shah NJ, Lippert T, Zilles K, Evans AC. BigBrain: An ultrahigh-resolution 3D human brain model. Science. 2013; doi: 10.1126/science.1235381.

Amunts K, Morosan P, Hilbig H, Zilles K. Auditory system. In: *The Human Nervous System* Elsevier; 2012.p. 1270–1300.

Andersson JLR, Jenkinson M, Smith S. Non-linear registration, aka spatial normalisation. FMRIB Technial Report TR07JA2.; 2007.

Andersson JLR, Skare S, Ashburner J. How to correct susceptibility distortions in spin-echo echo-planar images: application to diffusion tensor imaging. NeuroImage. 2003 oct; 20(2):870–88. doi: 10.1016/S1053-8119(03)00336-7.

Andersson JLR, Sotiropoulos SN. Non-parametric representation and prediction of single- and multi-shell diffusion-weighted MRI data using Gaussian processes. NeuroImage. 2015 nov; 122:166–76. doi: 10.1016/j.neuroimage.2015.07.067.

Andersson JLR, Sotiropoulos SN. An integrated approach to correction for off-resonance effects and subject movement in diffusion MR imaging. NeuroImage. 2016 jan; 125:1063–1078. doi: 10.1016/j.neuroimage.2015.10.019.

Ashburner J, Friston KJ. Unified segmentation. NeuroImage. 2005 jul; 26(3):839–851. doi: 10.1016/j.neuroimage.2005.02.018.

Avants BB, Tustison NJ, Song G, Cook PA, Klein A, Gee JC. A reproducible evaluation of ANTs similarity metric performance in brain image registration. NeuroImage. 2011 feb; 54(3):2033–44. http://www.ncbi.nlm.nih.gov/pubmed/20851191http://www.pubmedcentral.nih.gov/articlerender.fcgi?artid=PMC3065962, doi: 10.1016/j.neuroimage.2010.09.025.

Behrens TEJ, Berg HJ, Jbabdi S, Rushworth MFS, Woolrich MW. Probabilistic diffusion tractography with multiple fibre orientations: What can we gain? NeuroImage. 2007 jan; 34(1):144–55. http://www.ncbi.nlm.nih.gov/pubmed/17070705, doi: 10.1016/j.neuroimage.2006.09.018.

Brett M, Hanke M, Côté MA, Markiewicz C, Ghosh S, Wassermann D, Gerhard S, Larson E, Lee GR, Halchenko Y, Kastman E, M C, Morency FC, Maloney B, Rokem A, Cottaar M, Millman J, jaeilepp, Gramfort A, Vincent RD, et al. nipy/nibabel: 2.2.0. . 2017 Oct; https://doi.org/10.5281/zenodo.1011207, doi: 10.5281/zenodo.1011207.

Calabrese E, Hickey P, Hulette C, Zhang J, Parente B, Lad SP, Johnson GA. Postmortem diffusion MRI of the human brainstem and thalamus for deep brain stimulator electrode localization. Human brain mapping. 2015 aug; 36(8):3167–78. http://www.ncbi.nlm.nih.gov/pubmed/26043869http://www.pubmedcentral.nih.gov/articlerender.fcgi?artid=PMC4652933, doi: 10.1002/hbm.22836.

Manuscript submitted to eLife

De Martino F, Moerel M, van de Moortele PF, Ugurbil K, Goebel R, Yacoub E, Formisano E. Spatial organization of frequency preference and selectivity in the human inferior colliculus. Nature communications. 2013; 4:1386. http://www.ncbi.nlm.nih.gov/pubmed/23340426http://www.pubmedcentral.nih.gov/articlerender.fcgi?artid=PMC3556928, doi: 10.1038/ncomms2379.

De Martino F, Moerel M, Xu J, van de Moortele PF, Ugurbil K, Goebel R, Yacoub E, Formisano E. High-Resolution Mapping of Myeloarchitecture In Vivo: Localization of Auditory Areas in the Human Brain. Cerebral cortex (New York, NY : 1991). 2015 oct; 25(10):3394–405. http://www.ncbi.nlm.nih.gov/pubmed/24994817http://www.pubmedcentral.nih.gov/articlerender.fcgi?artid=PMC4585494, doi: 10.1093/cercor/bhu150.

De No RL. III. General Plan of Structure of the Primary Cochlear Nuclei. The Laryngoscope. 1933 apr; 43(4):327–349. http://doi.wiley.com/10.1288/00005537-193304000-00014, doi: 10.1288/00005537-193304000-00014.

De No RL. The central projection of the nerve endings of the internal ear. The Laryngoscope. 1933 jan; 43(1):1–38. http://doi.wiley.com/10.1288/00005537-193301000-00001, doi: 10.1288/00005537-193301000-00001.

Devlin JT, Sillery EL, Hall DA, Hobden P, Behrens TEJ, Nunes RG, Clare S, Matthews PM, Moore DR, Johansen-Berg H. Reliable identification of the auditory thalamus using multi-modal structural analyses. NeuroImage. 2006 may; 30(4):1112–20. http://www.ncbi.nlm.nih.gov/pubmed/16473021http://www.pubmedcentral.nih.gov/articlerender.fcgi?artid=PMC1458525, doi: 10.1016/j.neuroimage.2005.11.025.

Dhollander T, Raffelt D, Connelly A. Unsupervised 3-tissue response function estimation from single-shell or multi-shell diffusion MR data without a co-registered T1 image. In: *ISMRM Workshop on Breaking the Barriers of Diffusion MRI*; 2016. p. 5.

Dhollander T, Raffelt D, Connelly A. Unsupervised 3-tissue response function estimation from single-shell or multi-shell diffusion MR data without a co-registered T1 image. In: *Proceedings of the 26th annual meeting of the International Society of Magnetic Resonance in Medicine*; 2018. p. 1569.

Ding SL, Royall JJ, Sunkin SM, Ng L, Facer BAC, Lesnar P, Guillozet-Bongaarts A, McMurray B, Szafer A, Dolbeare TA, Stevens A, Tirrell L, Benner T, Caldejon S, Dalley RA, Dee N, Lau C, Nyhus J, Reding M, Riley ZL, et al. Comprehensive cellular-resolution atlas of the adult human brain. . 2016; doi: 10.1002/cne.24097.

Duvernoy HM. Human Brain Stem Vessels: Including the Pineal Gland and Information on Brain Stem Infarction, vol. 11. Springer Science & Business Media; 2013. https://books.google.com/books?id=K87sCAAAQBAJ{&}pgis=1.

Evans EF. Cochlear Nerve and Cochlear Nucleus. In: *Handbook of Sensory Physiology* Springer Berlin Heidelberg; 1975.p. 1–108. http://www.springerlink.com/index/10.1007/978-3-642-65995-9{_}1, doi: 10.1007/978-3-642-65995-9_1.

Fonov V, Evans AC, Botteron K, Almli CR, McKinstry RC, Collins DL. Unbiased average age-appropriate atlases for pediatric studies. NeuroImage. 2011; 54(1):313–327. http://dx.doi.org/10.1016/j.neuroimage.2010.07.033, doi: 10.1016/j.neuroimage.2010.07.033.

Fonov V, Evans A, McKinstry R, Almli C, Collins D. Unbiased nonlinear average age-appropriate brain templates from birth to adulthood. NeuroImage. 2009; 47:S102. http://linkinghub.elsevier.com/retrieve/pii/S1053811909708845, doi: 10.1016/S1053-8119(09)70884-5.

Friston KJ, Holmes AP, Worsley KJ, Poline JP, Frith CD, Frackowiak RSJ. Statistical parametric maps in functional imaging: A general linear approach. Human Brain Mapping. 1994; doi: 10.1002/hbm.460020402.

Garyfallidis E. Towards an accurate brain tractography. PhD thesis, University of Cambridge; 2013.

Garyfallidis E, Brett M, Amirbekian B, Rokem A, van der Walt S, Descoteaux M, Nimmo-Smith I, Dipy Contributors. Dipy, a library for the analysis of diffusion MRI data. Frontiers in neuroinformatics. 2014; 8:8. doi: 10.3389/fninf.2014.00008.

Glasser MF, Coalson TS, Robinson EC, Hacker CD, Harwell J, Yacoub E, Ugurbil K, Andersson J, Beckmann CF, Jenkinson M, Smith SM, Van Essen DC. A multi-modal parcellation of human cerebral cortex. Nature. 2016; doi: 10.1038/nature18933.

Glendenning KK, Masterton RB. Comparative Morphometry of Mammalian Central Auditory Systems: Variation in Nuclei and Form of the Ascending System. Brain Behav Evol. 1998; 51:59–89. http://www.karger.chhttp://biomednet.com/karger.

Manuscript submitted to eLife
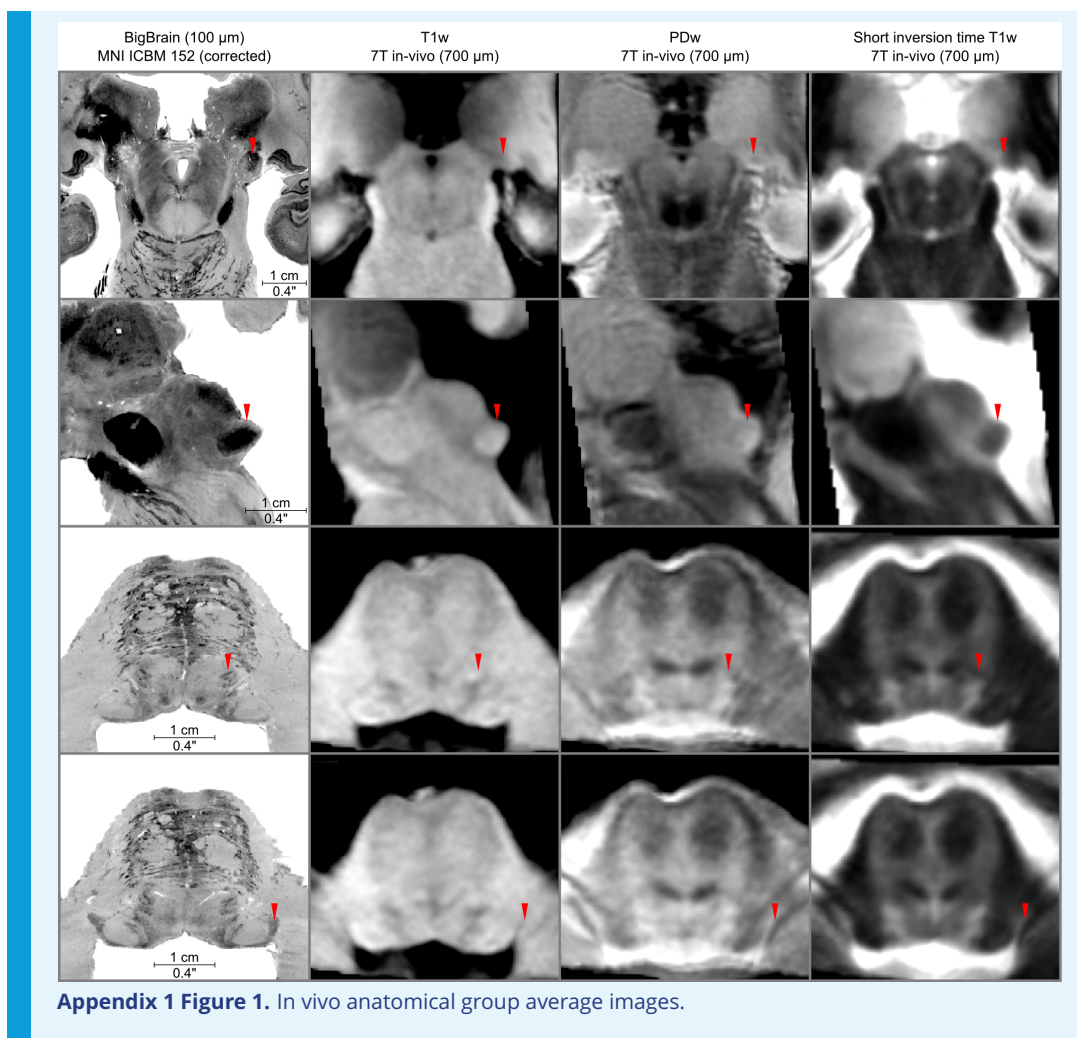
1069 **Goebel R**. BrainVoyager — Past, present, future. NeuroImage. 2012 aug; 62(2):748–756. doi:
1070 10.1016/j.neuroimage.2012.01.083.

1071 **Gorgolewski K**, Burns CD, Madison C, Clark D, Halchenko YO, Waskom ML, Ghosh SS. Nipype: a flexible,
1072 lightweight and extensible neuroimaging data processing framework in python. Front Neuroinform. 2011 08;
1073 5. https://doi.org/10.3389/fninf.2011.00013, doi: 10.3389/fninf.2011.00013.

1074 **Gray H**, Lewis W. Anatomy of the human body. 20 ed. Philadelphia: Lea \& Febiger; 1918.

1075 **Griffiths TD**, Uppenkamp S, Johnsrude I, Josephs O, Patterson RD. Encoding of the temporal regularity of sound
1076 in the human brainstem. Nature Neuroscience. 2001; doi: 10.1038/88459.

1077 **Griswold MA**, Jakob PM, Heidemann RM, Nittka M, Jellus V, Wang J, Kiefer B, Haase A. Generalized Autocalibrating
1078 Partially Parallel Acquisitions (GRAPPA). Magnetic Resonance in Medicine. 2002; 47(6):1202–1210. doi:
1079 10.1002/mrm.10171.

1080 **Guimaraes AR**, Melcher JR, Talavage TM, Baker JR, Ledden P, Rosen BR, Kiang NYS, Fullerton BC, Weisskoff RM.
1081 Imaging subcortical auditory activity in humans. Human Brain Mapping. 1998; 6(1):33–41. http://doi.wiley.
1082 com/10.1002/{%}28SICI{%}291097-0193{%}281998{%}296{%}3A1{%}3C33{%}3A{%}3AAID-HBM3{%}3E3.0.
1083 CO{%}3B2-M, doi: 10.1002/(SICI)1097-0193(1998)6:1<33::AID-HBM3>3.0.CO;2-M.

1084 **Gulban OF**, De Martino F, Vu AT, Yacoub E, Uğurbil K, Lenglet C. Cortical fibers orientation mapping using in-vivo
1085 whole brain 7 T diffusion MRI. NeuroImage. 2018 sep; 178(December 2017):104–118. http://linkinghub.elsevier.
1086 com/retrieve/pii/S1053811918304087https://linkinghub.elsevier.com/retrieve/pii/S1053811918304087, doi:
1087 10.1016/j.neuroimage.2018.05.010.

1088 **Gulban OF**, Schneider M, Marquardt I, Haast RAM, De Martino F. A scalable method to improve gray matter
1089 segmentation at ultra high field MRI. PLOS ONE. 2018 jun; 13(6):e0198335. http://dx.plos.org/10.1371/journal.
1090 pone.0198335, doi: 10.1371/journal.pone.0198335.

1091 **Harms MP**, Melcher JR. Sound repetition rate in the human auditory pathway: representations in the waveshape
1092 and amplitude of fMRI activation. Journal of neurophysiology. 2002 sep; 88(3):1433–50. http://www.ncbi.nlm.
1093 nih.gov/pubmed/12205164, doi: 10.1152/jn.2002.88.3.1433.

1094 **Hawley ML**, Melcher JR, Fullerton BC. Effects of sound bandwidth on fMRI activation in human
1095 auditory brainstem nuclei. Hearing research. 2005 jun; 204(1-2):101–10. http://www.ncbi.nlm.
1096 nih.gov/pubmed/15925195http://www.pubmedcentral.nih.gov/articlerender.fcgi?artid=PMC1855158, doi:
1097 10.1016/j.heares.2005.01.005.

1098 **Hawrylycz MJ**, Lein ES, Guillozet-Bongaarts AL, Shen EH, Ng L, Miller JA, van de Lagemaat LN, Smith KA,
1099 Ebbert A, Riley ZL, Abajian C, Beckmann CF, Bernard A, Bertagnolli D, Boe AF, Cartagena PM, Chakravarty
1100 MM, Chapin M, Chong J, Dalley RA, et al. An anatomically comprehensive atlas of the adult human brain
1101 transcriptome. Nature. 2012 sep; 489(7416):391–399. http://www.ncbi.nlm.nih.gov/pubmed/22996553http:
1102 //www.pubmedcentral.nih.gov/articlerender.fcgi?artid=PMC4243026, doi: 10.1038/nature11405.

1103 **Javad F**, Warren JD, Micallef C, Thornton JS, Golay X, Yousry T, Mancini L. Auditory tracts identified with
1104 combined fMRI and diffusion tractography. NeuroImage. 2014 jan; 84:562–74. http://www.ncbi.nlm.
1105 nih.gov/pubmed/24051357http://www.pubmedcentral.nih.gov/articlerender.fcgi?artid=PMC3898984, doi:
1106 10.1016/j.neuroimage.2013.09.007.

1107 **Jenkinson M**, Beckmann CF, Behrens TEJ, Woolrich MW, Smith SM. FSL. NeuroImage. 2012 aug; 62(2):782–790.
1108 doi: 10.1016/j.neuroimage.2011.09.015.

1109 **Jeurissen B**, Tournier JD, Dhollander T, Connelly A, Sijbers J. Multi-tissue constrained spherical deconvolution
1110 for improved analysis of multi-shell diffusion MRI data. NeuroImage. 2014 dec; 103:411–426. http://www.
1111 ncbi.nlm.nih.gov/pubmed/25109526, doi: 10.1016/j.neuroimage.2014.07.061.

1112 **Jiang ZD**, Moore DR, J King A. Sources of subcortical projections to the superior colliculus in the ferret. Brain
1113 Research. 1997 may; 755(2):279–292. http://linkinghub.elsevier.com/retrieve/pii/S0006899397001054, doi:
1114 10.1016/S0006-8993(97)00105-4.

1115 **Johnson GA**, Benveniste H, Black RD, Hedlund LW, Maronpot RR, Smith BR. Histology by magnetic resonance
1116 microscopy. Magnetic resonance quarterly. 1993 mar; 9(1):1–30. http://www.ncbi.nlm.nih.gov/pubmed/
1117 8512830, doi: 10.1139/m63-008.

1118 **Kay KN**, Rokem A, Winawer J, Dougherty RF, Wandell BA. GLMdenoise: A fast, automated technique for denoising
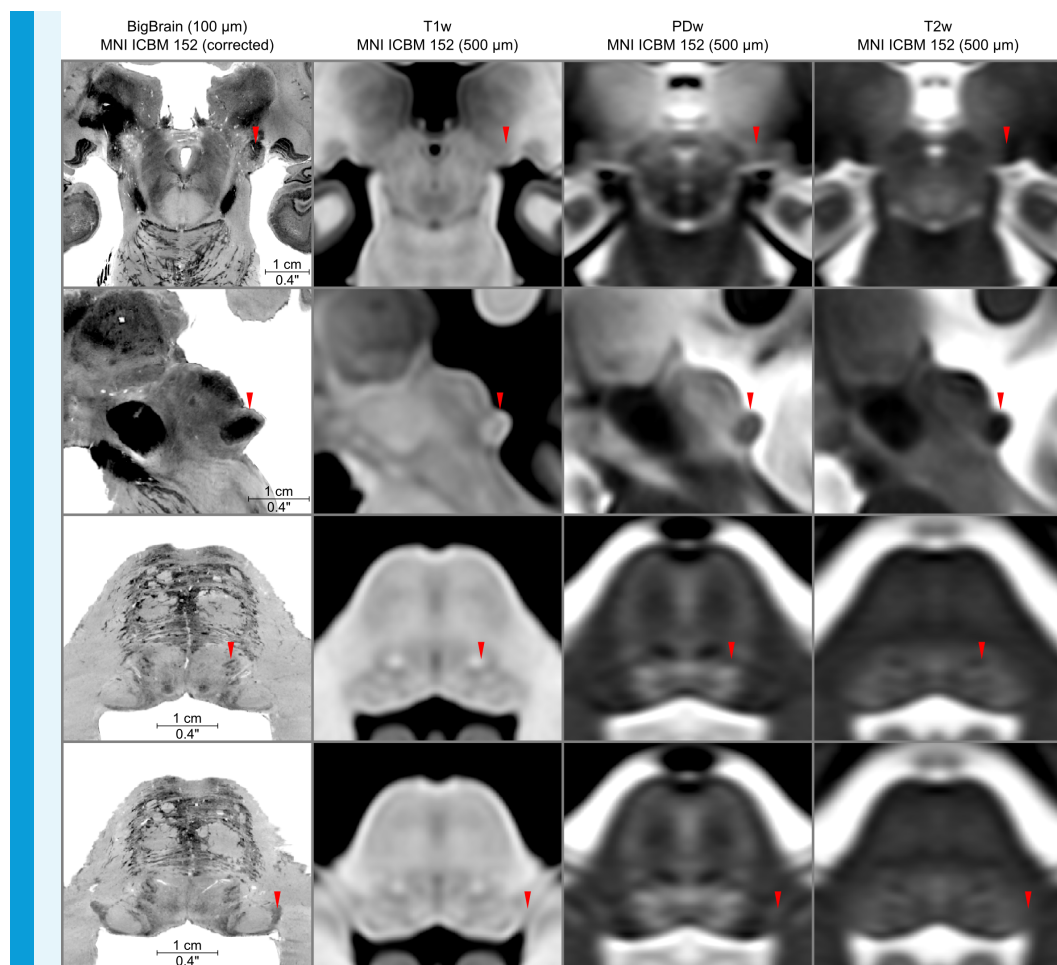1119 task-based fMRI data. Frontiers in Neuroscience. 2013; doi: 10.3389/fnins.2013.00247.

Kulesza RJ. Cytoarchitecture of the human superior olivary complex: medial and lateral superior olive. Hearing research. 2007 mar; 225(1-2):80–90. http://www.ncbi.nlm.nih.gov/pubmed/17250984, doi: 10.1016/j.heares.2006.12.006.

Kulesza RJ, Grothe B. Yes, there is a medial nucleus of the trapezoid body in humans. Frontiers in neuroanatomy. 2015 may; 9(5):35. http://www.ncbi.nlm.nih.gov/pubmed/4379933http://www.ncbi.nlm.nih.gov/pubmed/25873865http://www.pubmedcentral.nih.gov/articlerender.fcgi?artid=PMC4379933, doi: 10.3389/fnana.2015.00035.

Lévy B. A Numerical Algorithm for L 2 Semi-Discrete Optimal Transport in 3D. ESAIM: Mathematical Modelling and Numerical Analysis. 2015 nov; 49(6):1693–1715. http://www.esaim-m2an.org/10.1051/m2an/2015055, doi: 10.1051/m2an/2015055.

Lévy B, Schwindt EL. Notions of optimal transport theory and how to implement them on a computer. Computers and Graphics (Pergamon). 2018; doi: 10.1016/j.cag.2018.01.009.

Maffei C, Jovicich J, De Benedictis A, Corsini F, Barbareschi M, Chioffi F, Sarubbo S. Topography of the human acoustic radiation as revealed by ex vivo fibers micro-dissection and in vivo diffusion-based tractography. Brain structure & function. 2018 jan; 223(1):449–459. http://www.ncbi.nlm.nih.gov/pubmed/28866840, doi: 10.1007/s00429-017-1471-6.

Malmierca MS, Hackett TA. Structural organization of the ascending auditory pathway. The Auditory Brain. 2010; p. 9–41.

Merker B. Silver staining of cell bodies by means of physical development. Journal of Neuroscience Methods. 1983 nov; 9(3):235–241. http://linkinghub.elsevier.com/retrieve/pii/0165027083900869, doi: 10.1016/0165-0270(83)90086-9.

Miller KL, Stagg CJ, Douaud G, Jbabdi S, Smith SM, Behrens TEJ, Jenkinson M, Chance SA, Esiri MM, Voets NL, Jenkinson N, Aziz TZ, Turner MR, Johansen-Berg H, McNab JA. Diffusion imaging of whole, post-mortem human brains on a clinical MRI scanner. NeuroImage. 2011 jul; 57(1):167–181. http://www.pubmedcentral.nih.gov/articlerender.fcgi?artid=PMC3115068, doi: 10.1016/j.neuroimage.2011.03.070.

Moeller S, Yacoub E, Olman CA, Auerbach E, Strupp J, Harel N, Uğurbil K. Multiband multislice GE-EPI at 7 tesla, with 16-fold acceleration using partial parallel imaging with application to high spatial and temporal whole-brain fMRI. Magnetic resonance in medicine. 2010 may; 63(5):1144–53. http://www.ncbi.nlm.nih.gov/pubmed/20432285http://www.pubmedcentral.nih.gov/articlerender.fcgi?artid=PMC2906244, doi: 10.1002/mrm.22361.

Moerel M, De Martino F, Uğurbil K, Yacoub E, Formisano E. Processing of frequency and location in human subcortical auditory structures. Scientific reports. 2015 nov; 5:17048. doi: 10.1038/srep17048.

Moore JK. The human auditory brain stem: a comparative view. Hearing research. 1987; 29:1–32. doi: 10.1016/0378-5955(87)90202-4.

Moore JK, Perazzo LM, Braun A. Time course of axonal myelination in the human brainstem auditory pathway. Hearing research. 1995 jul; 87(1-2):21–31. http://www.ncbi.nlm.nih.gov/pubmed/8567438, doi: 10.1016/0378-5955(95)00218-9.

Mori S, Crain BJ, Chacko VP, van Zijl PC. Three-dimensional tracking of axonal projections in the brain by magnetic resonance imaging. Annals of neurology. 1999 feb; 45(2):265–9. http://www.ncbi.nlm.nih.gov/pubmed/9989633, doi: 10.1002/1531-8249(199902)45:2<265::AID-ANA21>3.0.CO;2-3.

Paxinos G, T F, C W. Human Brainstem: Cytoarchitecture, Chemoarchitecture, Myeloarchitecture. 1 ed. Acedemic Press; 2019.

Pfefferbaum A, Sullivan EV, Adalsteinsson E, Garrick T, Harper C. Postmortem MR imaging of formalin-fixed human brain. NeuroImage. 2004 apr; 21(4):1585–95. http://www.ncbi.nlm.nih.gov/pubmed/15050582, doi: 10.1016/j.neuroimage.2003.11.024.

Reveley C, Seth AK, Pierpaoli C, Silva AC, Yu D, Saunders RC, Leopold DA, Ye FQ. Superficial white matter fiber systems impede detection of long-range cortical connections in diffusion MR tractography. Proceedings of the National Academy of Sciences of the United States of America. 2015 may; 112(21):E2820–8. http://www.ncbi.nlm.nih.gov/pubmed/25964365http://www.pubmedcentral.nih.gov/articlerender.fcgi?artid=PMC4450402, doi: 10.1073/pnas.1418198112.

Rose J, Galambos R, Hughes J. Organization of frequency sensitive neurons in the cochlear nuclear complex of the cat. In: *Neural Mechanisms of the Auditory and Vestibular Systems* Thomas Springfield, IL; 1960.p. 116–136. http://scholar.google.com/scholar?hl=en{&}btnG=Search{&}q=intitle:Organization+of+frequency+ sensitive+neurons+in+the+cochlear+nuclear+complex+of+the+cat{#}0.

Ryugo DK, May SK. The projections of intracellularly labeled auditory nerve fibers to the dorsal cochlear nucleus of cats. The Journal of comparative neurology. 1993 mar; 329(1):20–35. http://www.ncbi.nlm.nih.gov/pubmed/ 8454724, doi: 10.1002/cne.903290103.

Ryugo DK, Parks TN. Primary innervation of the avian and mammalian cochlear nucleus. Brain Research Bulletin. 2003; 60(5-6):435–456. doi: 10.1016/S0361-9230(03)00049-2.

Sando I. The Anatomical Interrelationships of the Cochlear Nerve Fibers. Acta Oto-Laryngologica. 1965 jan; 59(2-6):417–436. http://www.tandfonline.com/doi/full/10.3109/00016486509124577, doi: 10.3109/00016486509124577.

Schilling KG, Daducci A, Maier-Hein K, Poupon C, Houde JC, Nath V, Anderson AW, Landman BA, Descoteaux M. Challenges in diffusion MRI tractography - Lessons learned from international benchmark competitions. Magnetic resonance imaging. 2019 apr; 57:194–209. http://www.ncbi.nlm.nih.gov/pubmed/30503948http: //www.pubmedcentral.nih.gov/articlerender.fcgi?artid=PMC6331218, doi: 10.1016/j.mri.2018.11.014.

Schilling KG, Nath V, Hansen C, Parvathaneni P, Blaber J, Gao Y, Neher P, Aydogan DB, Shi Y, Ocampo-Pineda M, Schiavi S, Daducci A, Girard G, Barakovic M, Rafael-Patino J, Romascano D, Rensonnet G, Pizzolato M, Bates A, Fischi E, et al. Limits to anatomical accuracy of diffusion tractography using modern approaches. NeuroImage. 2019; doi: 10.1016/j.neuroimage.2018.10.029.

Schofield BR. Structural organization of the descending auditory pathway. The Auditory Brain. 2010; p. 43–64.

Setsompop K, Gagoski BA, Polimeni JR, Witzel T, Wedeen VJ, Wald LL. Blipped-controlled aliasing in par- allel imaging for simultaneous multislice echo planar imaging with reduced g-factor penalty. Magnetic resonance in medicine. 2012 may; 67(5):1210–24. http://www.ncbi.nlm.nih.gov/pubmed/21858868http: //www.pubmedcentral.nih.gov/articlerender.fcgi?artid=PMC3323676, doi: 10.1002/mrm.23097.

Sigalovsky IS, Melcher JR. Effects of sound level on fMRI activation in human brainstem, thalamic and cortical centers. Hearing research. 2006 may; 215(1-2):67–76. http://www.ncbi.nlm.nih.gov/pubmed/16644153http: //www.pubmedcentral.nih.gov/articlerender.fcgi?artid=PMC1794213, doi: 10.1016/j.heares.2006.03.002.

Sotiropoulos SN, Jbabdi S, Xu J, Andersson JL, Moeller S, Auerbach EJ, Glasser MF, Hernandez M, Sapiro G, Jenkinson M, Feinberg DA, Yacoub E, Lenglet C, Van Essen DC, Ugurbil K, Behrens TEJ. Advances in diffusion MRI acquisition and processing in the Human Connectome Project. NeuroImage. 2013; doi: 10.1016/j.neuroimage.2013.05.057.

Sparks DL, Hartwich-Young R. The deep layers of the superior colliculus. Reviews of oculomotor research. 1989; 3:213–55. http://www.ncbi.nlm.nih.gov/pubmed/2486324.

Strominger NL, Hurwitz JL. Anatomical aspects of the superior olivary complex. The Journal of comparative neu- rology. 1976 dec; 170(4):485–97. http://www.ncbi.nlm.nih.gov/pubmed/826550, doi: 10.1002/cne.901700407.

Teeuwisse WM, Brink WM, Webb AG. Quantitative assessment of the effects of high-permittivity pads in 7 tesla MRI of the brain. Magnetic resonance in medicine. 2012; 67(5):1285–1293.

Thomas C, Ye FQ, Irfanoglu MO, Modi P, Saleem KS, Leopold DA, Pierpaoli C. Anatomical accuracy of brain con- nections derived from diffusion MRI tractography is inherently limited. Proceedings of the National Academy of Sciences. 2014 nov; 111(46):16574–16579. http://www.pnas.org/lookup/doi/10.1073/pnas.1405672111, doi: 10.1073/pnas.1405672111.

Tourdias T, Saranathan M, Levesque IR, Su J, Rutt BK. Visualization of intra-thalamic nuclei with opti- mized white-matter-nulled MPRAGE at 7T. NeuroImage. 2014 jan; 84:534–45. http://www.ncbi.nlm. nih.gov/pubmed/24018302http://www.pubmedcentral.nih.gov/articlerender.fcgi?artid=PMC3927795, doi: 10.1016/j.neuroimage.2013.08.069.

Tournier JD, Calamante F, Connelly A. Robust determination of the fibre orientation distribution in diffu- sion MRI: Non-negativity constrained super-resolved spherical deconvolution. NeuroImage. 2007; doi: 10.1016/j.neuroimage.2007.02.016.

1218 **Tournier JD**, Calamante F, Gadian DG, Connelly A. Direct estimation of the fiber orientation density
1219 function from diffusion-weighted MRI data using spherical deconvolution. NeuroImage. 2004; doi:
1220 10.1016/j.neuroimage.2004.07.037.

1221 **Triantafyllou C**, Polimeni JR, Keil B, Wald LL. Coil-to-coil physiological noise correlations and their impact on
1222 functional MRI time-series signal-to-noise ratio. Magnetic Resonance in Medicine. 2016 dec; 76(6):1708–1719.
1223 http://doi.wiley.com/10.1002/mrm.26041, doi: 10.1002/mrm.26041.

1224 **Ugurbil K**. What is feasible with imaging human brain function and connectivity using functional mag-
1225 netic resonance imaging. Philosophical Transactions of the Royal Society B: Biological Sciences. 2016
1226 oct; 371(1705):20150361. http://rstb.royalsocietypublishing.org/lookup/doi/10.1098/rstb.2015.0361, doi:
1227 10.1098/rstb.2015.0361.

1228 **Ugurbil K**, Adriany G, Andersen P, Chen W, Garwood M, Gruetter R, Henry PG, Kim SG, Lieu H, Tkac I, Vaughan
1229 T, Van De Moortele PF, Yacoub E, Zhu XH. Ultrahigh field magnetic resonance imaging and spectroscopy.
1230 Magnetic Resonance Imaging. 2003 dec; 21(10):1263–1281. https://linkinghub.elsevier.com/retrieve/pii/
1231 S0730725X03003382, doi: 10.1016/j.mri.2003.08.027.

1232 **Van de Moortele PF**, Auerbach EJ, Olman C, Yacoub E, Uğurbil K, Moeller S. T1 weighted brain images at 7
1233 Tesla unbiased for Proton Density, T2* contrast and RF coil receive B1 sensitivity with simultaneous vessel
1234 visualization. NeuroImage. 2009 jun; 46(2):432–46. doi: 10.1016/j.neuroimage.2009.02.009.

1235 **Van Der Walt S**, Colbert SC, Varoquaux G. The NumPy array: a structure for efficient numerical computation.
1236 Computing in Science & Engineering. 2011; 13(2):22–30.

1237 **Vaughan JT**, Garwood M, Collins CM, Liu W, DelaBarre L, Adriany G, Andersen P, Merkle H, Goebel R, Smith
1238 MB, Ugurbil K. 7T vs. 4T: RF power, homogeneity, and signal-to-noise comparison in head images. Mag-
1239 netic resonance in medicine. 2001 jul; 46(1):24–30. http://www.ncbi.nlm.nih.gov/pubmed/11443707, doi:
1240 10.1002/mrm.1156.

1241 **Vu AT**, Auerbach E, Lenglet C, Moeller S, Sotiropoulos SN, Jbabdi S, Andersson J, Yacoub E, Ugurbil K. High
1242 resolution whole brain diffusion imaging at 7T for the Human Connectome Project. NeuroImage. 2015; doi:
1243 10.1016/j.neuroimage.2015.08.004.

1244 **Wallace MN**, Cronin MJ, Bowtell RW, Scott IS, Palmer AR, Gowland PA. Histological Basis of Laminar MRI
1245 Patterns in High Resolution Images of Fixed Human Auditory Cortex. Frontiers in neuroscience. 2016 oct;
1246 10:455. http://www.ncbi.nlm.nih.gov/pubmed/27774049http://www.pubmedcentral.nih.gov/articlerender.
1247 fcgi?artid=PMC5054214, doi: 10.3389/fnins.2016.00455.

1248 **Wang N**, Anderson RJ, Badea A, Cofer G, Dibb R, Qi Y, Johnson GA. Whole mouse brain structural connectomics
1249 using magnetic resonance histology. Brain structure & function. 2018 dec; 223(9):4323–4335. http://www.
1250 ncbi.nlm.nih.gov/pubmed/30225830, doi: 10.1007/s00429-018-1750-x.

1251 **Wang R**, Benner T, Sorensen AG, Wedeen VJ. Diffusion toolkit: a software package for diffusion imaging data
1252 processing and tractography. In: *Proc Intl Soc Mag Reson Med* Berlin; 2007. p. 3720.

1253 **Webster DB**. An Overview of Mammalian Auditory Pathways with an Emphasis on Humans. In: *Handbook
1254 of Auditory Research* Springer; 1992.p. 1–22. http://link.springer.com/10.1007/978-1-4612-4416-5{_}1, doi:
1255 10.1007/978-1-4612-4416-5_1.

1256 **Winer Ja**. The human medial geniculate body. Hearing Research. 1984; 15(3):225–247. doi: 10.1016/0378-
1257 5955(84)90031-5.

1258 **Yushkevich PA**, Piven J, Hazlett HC, Smith RG, Ho S, Gee JC, Gerig G. User-guided 3D active contour segmentation
1259 of anatomical structures: significantly improved efficiency and reliability. NeuroImage. 2006 jul; 31(3):1116–28.
1260 doi: 10.1016/j.neuroimage.2006.01.015.

Manuscript submitted to eLife

Appendix 1

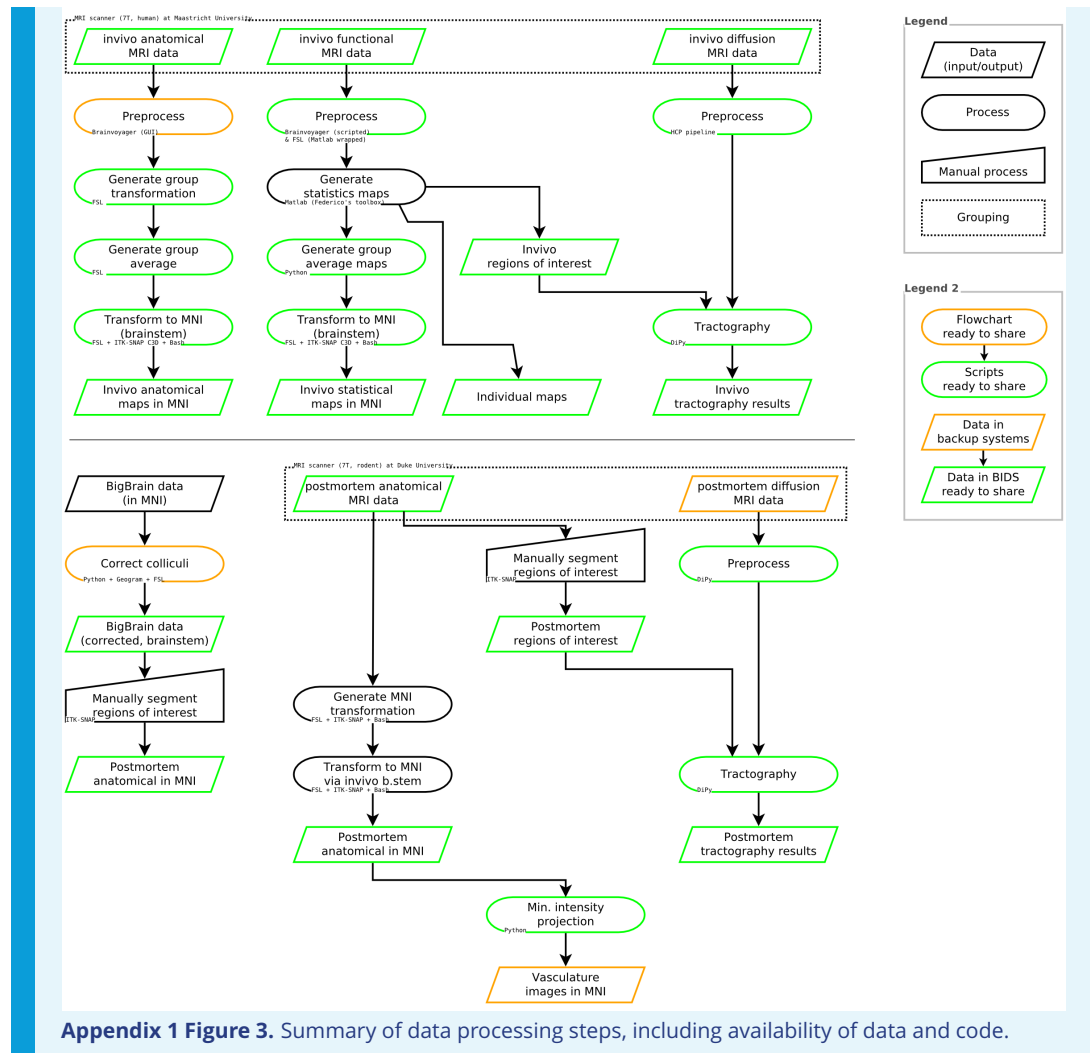**Appendix 1 Figure 1.** In vivo anatomical group average images.

Manuscript submitted to eLife

Appendix 1 Figure 2. Anatomical images from MNI ICBM 152 dataset compared to BigBrain histology in MNI152 space (left column).

1265

1266

1267

Appendix 1 Figure 3. Summary of data processing steps, including availability of data and code.

1269

1270

Manuscript submitted to eLife

number of streamlines (n = 7609)

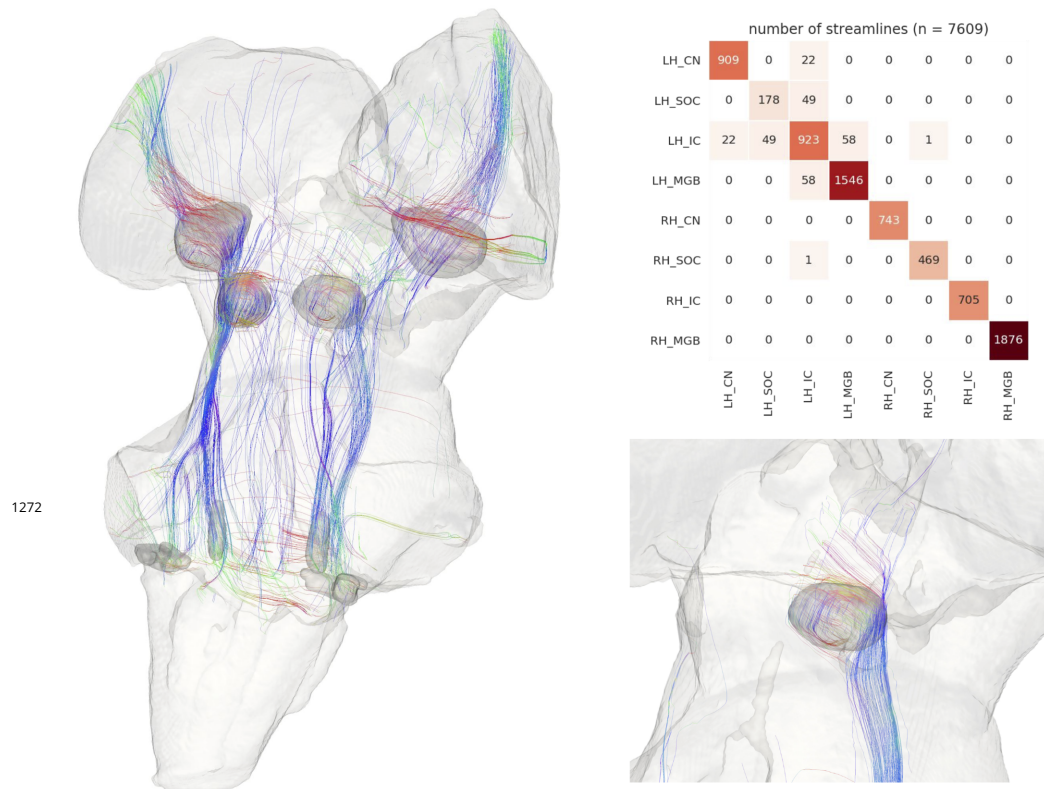|	LH_CN	LH_SOC	LH_IC	LH_MGB	RH_CN	RH_SOC	RH_IC	RH_MGB
LH_CN	909	0	22	0	0	0	0	0
LH_SOC	0	178	49	0	0	0	0	0
LH_IC	22	49	923	58	0	1	0	0
LH_MGB	0	0	58	1546	0	0	0	0
RH_CN	0	0	0	0	743	0	0	0
RH_SOC	0	0	1	0	0	469	0	0
RH_IC	0	0	0	0	0	0	705	0
RH_MGB	0	0	0	0	0	0	0	1876

1272

Figure 4–Figure supplement 1. Post mortem human diffusion-weighted MRI tractography (from 200 μm isotropic voxels) with anatomically defined subcortical auditory seeds, downsampled to 200 μm but undilated. Streamlines that passed through manual segmentations of the medulla and optic tracts were excluded. 10 percent of streamlines are visualized for clarity. Top right: connectivity heatmap of subcortical auditory structures. Bottom right: Streamlines that pass through the right inferior colliculus.
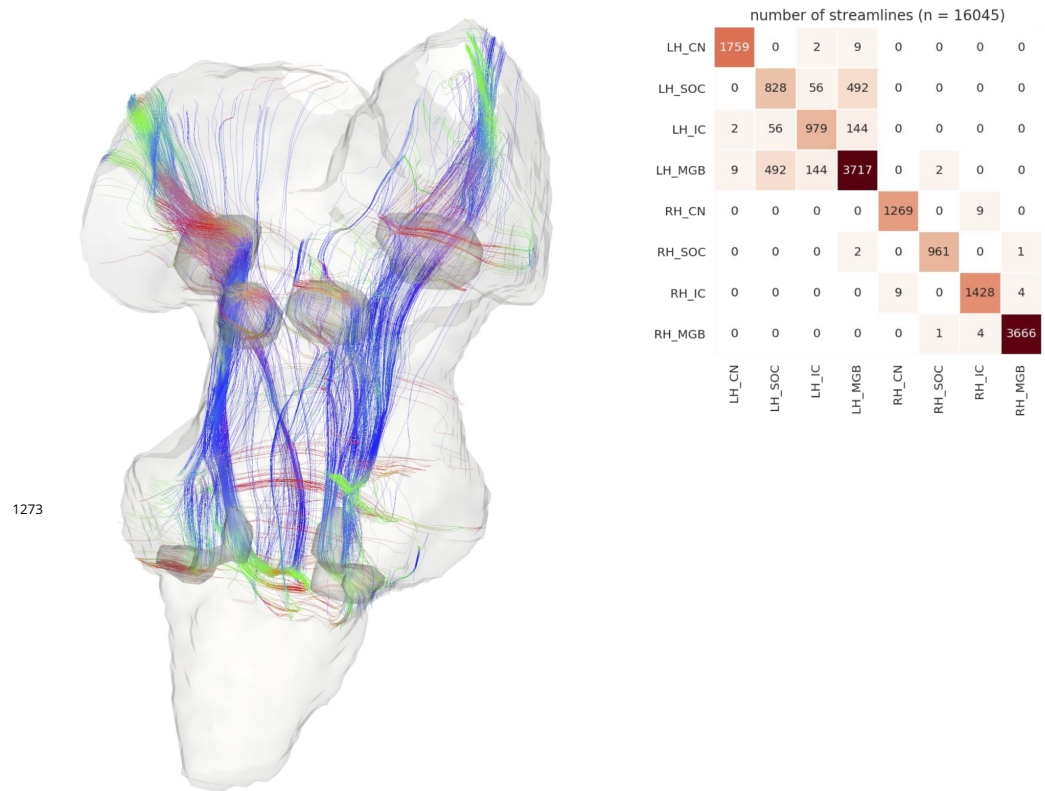
number of streamlines (n = 16045)

	LH_CN	LH_SOC	LH_IC	LH_MGB	RH_CN	RH_SOC	RH_IC	RH_MGB
LH_CN	1759	0	2	9	0	0	0	0
LH_SOC	0	828	56	492	0	0	0	0
LH_IC	2	56	979	144	0	0	0	0
LH_MGB	9	492	144	3717	0	2	0	0
RH_CN	0	0	0	0	1269	0	9	0
RH_SOC	0	0	0	2	0	961	0	1
RH_IC	0	0	0	0	9	0	1428	4
RH_MGB	0	0	0	0	0	1	4	3666

1273

Figure 4–Figure supplement 2. Post mortem human diffusion-weighted MRI tractography with anatomically defined subcortical auditory seeds. MRI data were downsampled from 200 μm to 1050 μm to match in vivo data acquisition and then processed in the same manner as other diffusion tractography analyses. Streamlines that passed through manual segmentations of the medulla and optic tracts were excluded. 10 percent of streamlines are visualized for clarity. Top right: Connectivity heatmap of subcortical auditory structures.
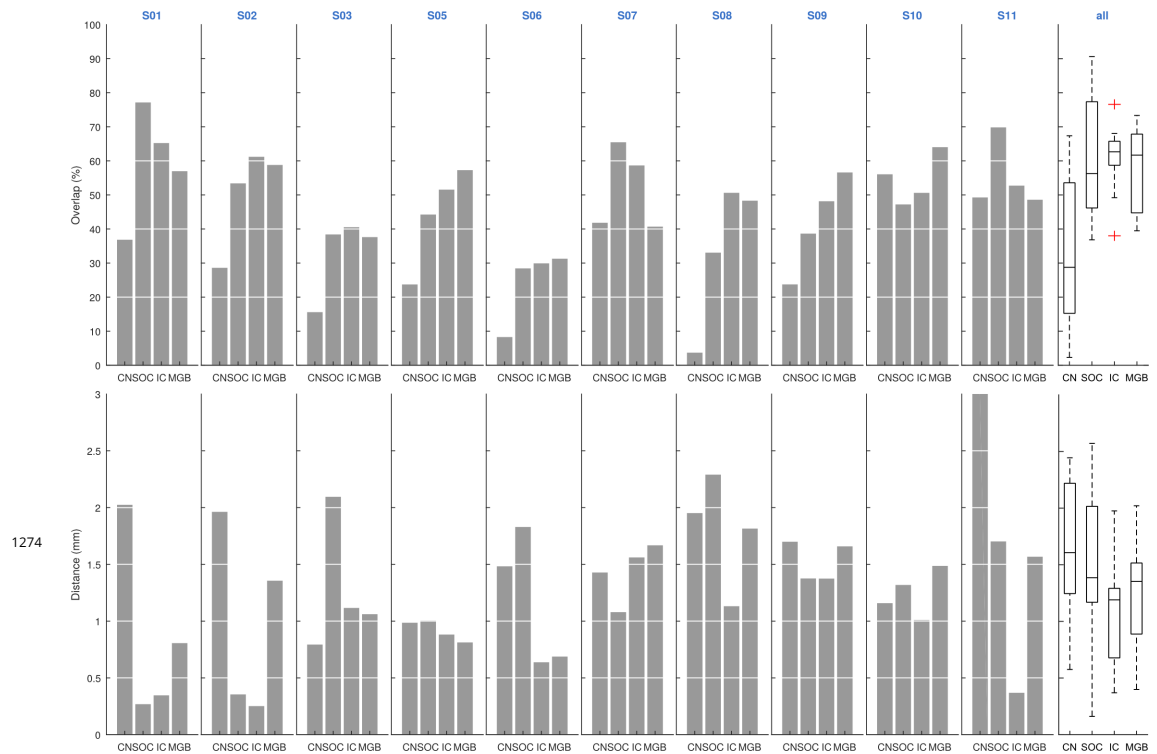
Figure 5–Figure supplement 1. Correspondence between single subject activation maps and leave-one-out functional probabilistic maps. Leave-one-out probabilistic functional maps are thresholded to identify voxels that are significantly responding to sounds in at least three of nine participants. The overlap represents (per region of interest) the percentage of the voxels on the leave-one-out probabilistic maps that is significantly responding to sounds in the left out subject. For each region of interest we also report the distance in mm between the centroids of the leave-one-out probabilistic maps and the centroids of the regions significantly responding to sounds in the left out subject. The last column represents the average overlap and distance across participants per region and error bars represent the standard error across the participants.
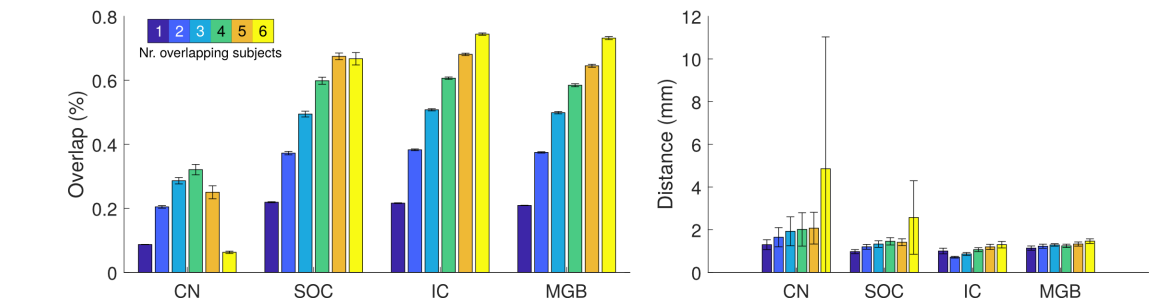

Figure 5–Figure supplement 2. Correspondence between single subject activation maps and leave-one-out functional probabilistic maps at different thresholds. Leave-one-out probabilistic functional maps are thresholded to identify voxels that are significantly responding to sounds by varying thresholds from at least one of nine participants to at least six of nine participants. The overlap represents (per region of interest) the percentage of the voxels on the leave-one-out probabilistic maps that is significantly responding to sounds in the left out subject. For each region of interest we also report the distance in mm between the centroids of the leave-one-out probabilistic maps and the centroids of the regions significantly responding to sounds in the left out subject. Boxplots represent the average overlap and distance across participants per region and error bars represent the standard error across the participants.
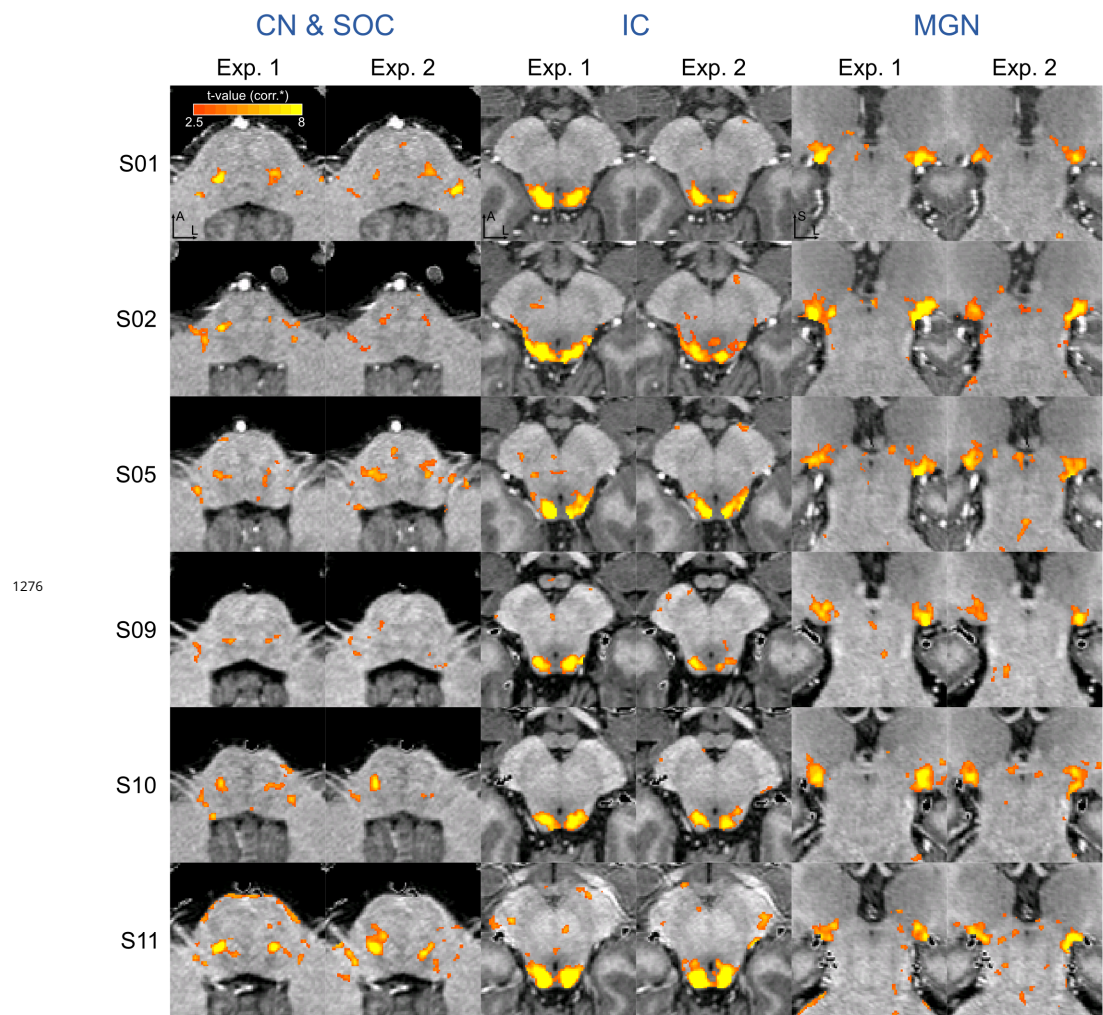
Figure 5–Figure supplement 3. Reproducibility of functional activation maps. Functional activation maps obtained from Experiment 1 and Experiment 2 (six participants) thresholded for significance (FDR-q = 0.05 and p<0.001; see Methods for details). For each participant, CN/SOC and IC are shown in transversal cuts, MGB is shown in a coronal cut.
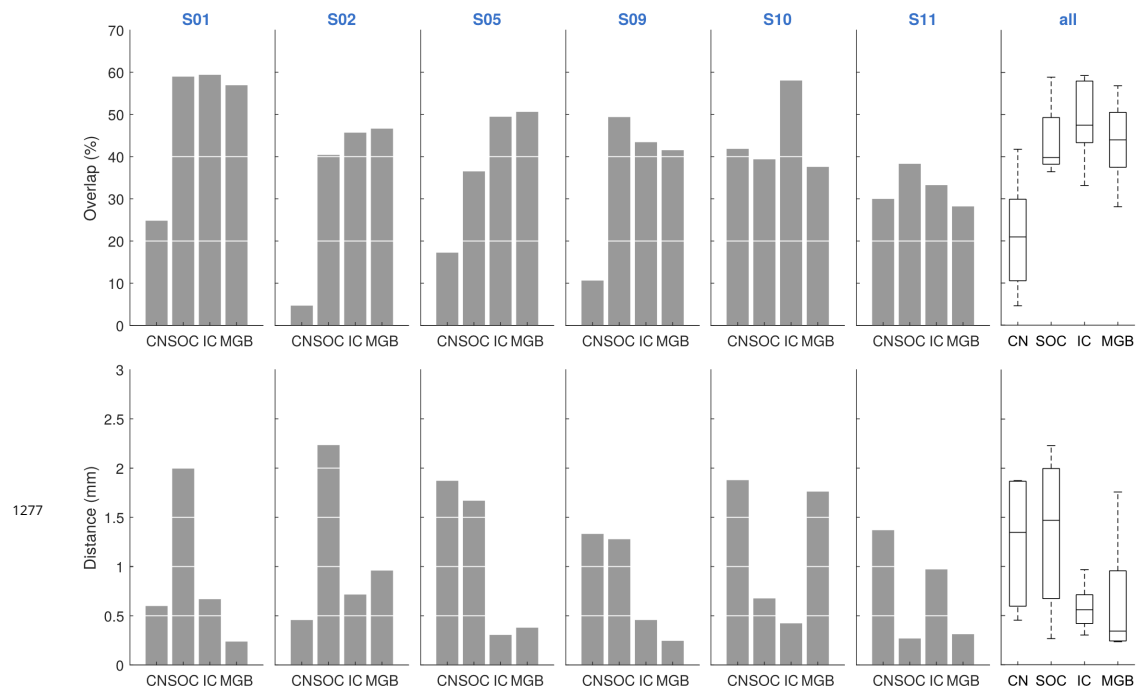
Manuscript submitted to eLife

Figure 5–Figure supplement 4. Correspondence between single subject activation maps Experiment 1 and Experiment 2. All maps are thresholded for significance (FDR-q=0.05 and p<0.001; see methods for details). The overlap represents (per region of interest) the percentage of the voxels significantly active in Experiment 1 that is significantly responding to sounds in Experiment 2. For each region of interest we also report the distance in mm between the centroids of the regions significantly responding to sounds in both experiments. Videos are provided in the appendix that visualize thresholded and unthresholded maps for each of the individual participants. The last column represents the average overlap and distance across participants per region and error bars represent the standard error across the participants.
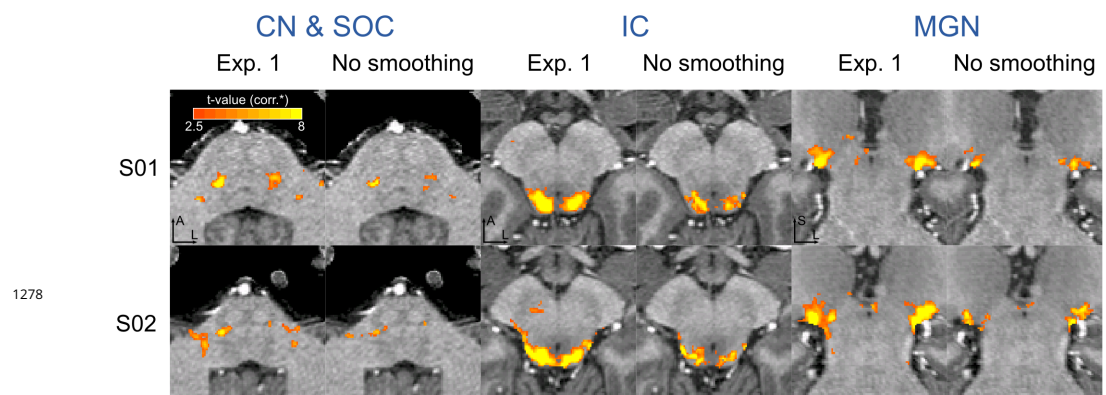

Figure 5–Figure supplement 5. Effect of spatial smoothing on functional activation maps. Functional activation maps obtained from Experiment 1 in two participants with and without applying spatial smoothing (1.5mm FWHM Gaussian smoothing) prior to the statistical analysis. Maps are thresholded for statistical significance (FDR-q = 0.05 & p<0.001; see Methods for details)). For each participant, CN/SOC and IC are shown in transversal cuts, MGB is shown in a coronal cut.
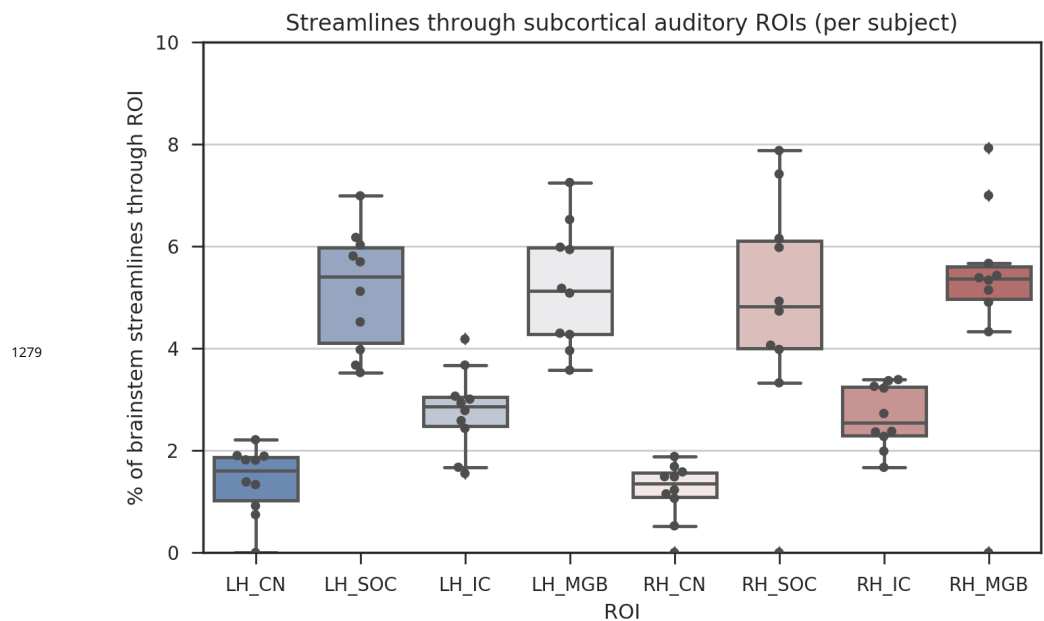
Figure 7–Figure supplement 1. Diffusion-weighted MRI tractography streamlines passing through each subcortical auditory region of interest for the ten in vivo participants. Bars represent 95% confidence intervals.